nanomaterials

MDPI

Review

Nanostructured MnO_2 as Electrode Materials for Energy Storage

Christian M. Julien * and Alain Mauger

Institut de Minéralogie, de Physique des Matériaux et de Cosmochimie (IMPMC),
Unité Mixte de Recherche 7590, Sorbonne Universités, 75005 Paris, France; alain.mauger@impmc.jussieu.fr
* Correspondence: christian.julien@upmc.fr; Tel.: +33-144-272-443

Received: 14 October 2017; Accepted: 5 November 2017; Published: 17 November 2017

Abstract: Manganese dioxides, inorganic materials which have been used in industry for more than a century, now find great renewal of interest for storage and conversion of energy applications. In this review article, we report the properties of MnO_2 nanomaterials with different morphologies. Techniques used for the synthesis, structural, physical properties, and electrochemical performances of periodic and aperiodic frameworks are discussed. The effect of the morphology of nanosized MnO_2 particles on their fundamental features is evidenced. Applications as electrodes in lithium batteries and supercapacitors are examined.

Keywords: energy storage and conversion; nanomaterials; MnO_2; lithium batteries; supercapacitors

1. Introduction

In recent years, intense Research & Development input on nanotechnology has delivered nano-objects (particles with size ≈ 100 nm or less) that possess a rich combination of physical properties, inasmuch as they differ from those of the bulk and depend on polymorphism, morphology, size of particles, size distribution, coating, and the precursor used in the synthesis [1]. With the need for renewable energies, these nano-substances have undergone extensive research, in order to develop new systems that can be used for energy storage and/or conversion. Among them, transition-metal oxides including TiO_2, MnO_2, V_2O_5, etc. are stable and robust materials with tunable properties offering large surface areas.

In the early ages, mineral manganese dioxides (MDOs) were used as black pigments for rock-art painting in paleolithic caves of the Magdalenian culture [2]; they can be considered as the first nanomaterials used up until then by human civilization. Today MnO_2 is an important functional metal oxide, which is technologically attractive for applications in different fields such as catalysts [3–5], absorbent of toxic metals [6], ion-sieves, molecular-sieves [7], artificial oxidase [8], component of the dry cell (Leclanché cell) [9], inorganic pigment in ceramics, electrodes for electrochemical batteries (lithium, magnesium, sodium) [10–13], and electrodes for supercapacitors [14,15]. MnO_2 has also been widely used in Duracell (alkaline) based barriers, photocatalytic activities, and electrolysis. Owing to its ability to absorb toxic ions, MnO_2 has been also found to have important applications in water-cleaning [16,17]. MDOs are non-stoichiometric compounds, because of inevitable structural water molecules that are physisorbed.

The engineering of manganese oxides used for energy storage and conversion has become more and more important to the point where a huge number of works is devoted to these materials. The great interest of MnO_2 as an inorganic material in the battery industry is due to its theoretical capacity (308 $mAh{\cdot}g^{-1}$ comparable to 270 $mAh{\cdot}g^{-1}$ of $LiCoO_2$) and capacitance (1370 $F{\cdot}g^{-1}$), natural abundance, low cost, and low toxicity [1]. MDOs crystallize with various morphologies and crystallographic forms including the α-, β-, γ-, δ- ε-, λ- and R-polymorphs, which are naturally

occurring minerals such as hollandite (2 × 2), pyrolusite (1 × 1), nsutite (1 × 1)/(1 × 2) with hexagonal (hex.) structure, birnessite (1 × ∞), akhtenkite (dense stack), spinel (1 × 1), and ramsdellite (1 × 2), respectively, where ($m \times n$) denotes the tunnel dimension. The polymorphism is due to the different ways of linking the MnO_6 octahedral architectonic units through corner- or edge-sharing that show variations in the chain and tunnel structures (see Figure 1) [18]. For example, the (3 × 3) tunnel structure of todorokite-type MnO_2 (octahedral molecular sieve labeled OMS-1) has a pore size of about 6.9 Å [7]. Note that the hollandite, cryptomelane, and coronadite minerals that are structurally related to (2 × 2) tunnel materials have water and different cation contents such as Ba^{2+}, K^+, and Pb^{2+}, respectively [19]. Consequently, properties of MDOs depend strongly on the crystalline structure, particle size, and morphology. The crystallographic data of some MDO compounds are summarized in Table 1.

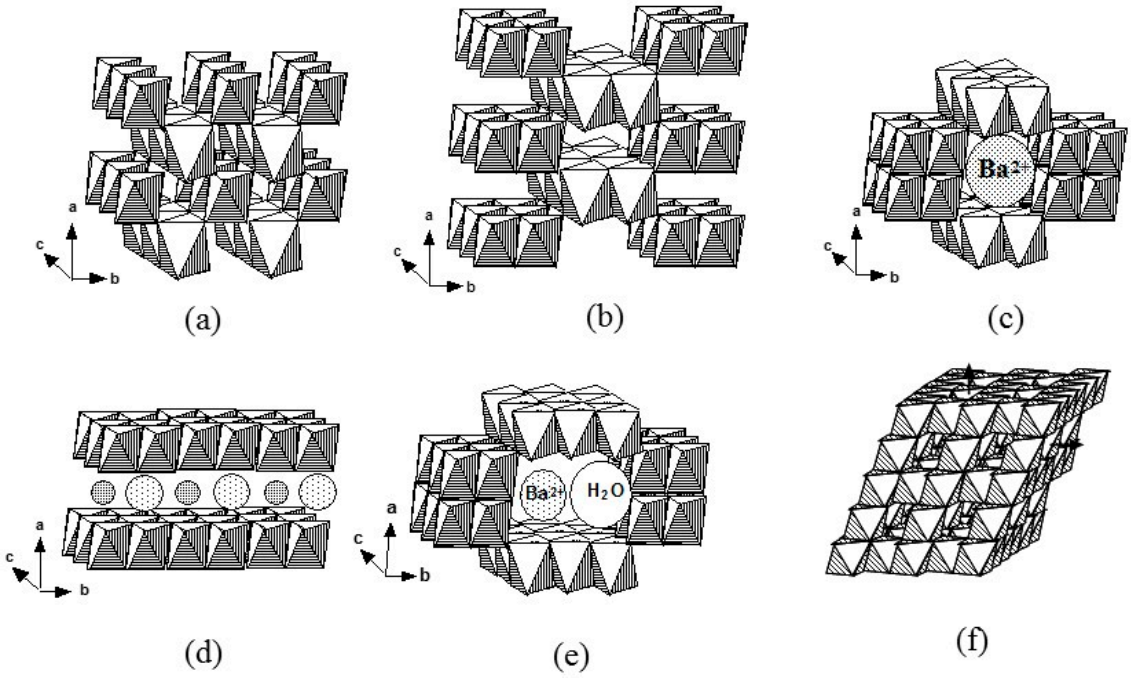

Figure 1. Representation of the different MnO_2 frameworks characterized by their tunnel ($m \times n$) structures. (**a**) pyrolusite (1 × 1); (**b**) ramsdellite (1 × 2); (**c**) hollandite (2 × 2); (**d**) birnessite (1 × ∞); (**e**) romanechite (2 × 3); and (**f**) spinel (1 × 1). Reproduced with permission from [18]. Elsevier, 2004.

Since MnO_2 was introduced as a depolarizing element in zinc-alkaline cells, a major step was realized with the utilization of natural and synthesized materials such as electrochemically (EMD), chemically (CMD), and heat-treated (HTMD) prepared MnO_2. All these frameworks are generally classified as members of the nsutite group: the γ-MnO_2 and ε-MnO_2 phases, distinguished by the quality of their X-ray diffraction diagrams [9]. Direct synthesis of EMD or CMD results in structural defects: (i) the "De Wolff defects" (denoted Pr) are intergrowth of pyrolusite in the ramsdellite matrix and (ii) the micro-twinning defects (denoted Tw). Figure 2 shows the degree of micro-twinnings as a function of the pyrolusite intergrowth in synthesized CMD, EMD, and HTMD manganese dioxides. In commercial EMD powders, Pr and Tw are close to 45–55% and 80–100%, respectively. Being relatively cheap, EMD materials are widely employed as electrodes in primary alkaline batteries and supercapacitors. EMD powders with manganese-cake microstructure (predominantly γ-MnO_2 phase) deliver a specific discharge capacity of 280 $mAh{\cdot}g^{-1}$ using 9 $mol{\cdot}L^{-1}$ KOH electrolyte [20]. An extensive review devoted to electrolytic MnO_2 has been published recently [21]. Therefore, we simply direct the readers to this review for specific properties of EMD, and attention in the present work is thus focused on other syntheses and related MnO_2 in the other α- and β-phases [21].

For the same reason, we did not detail any discussion on the MnO_2-based supercapacitors, because a 43-page review on them, including experimental aspects and discussion, prospective, has been recently published [22]. Consequently, we made the choice to focus the present work on the other major application of the MDOs, namely their use as active cathode elements of Li-ion batteries, in relation to the synthesis, structural, and morphological aspects of the nano-sized particles. Special attention has been paid to the synthesis aspect of the MDOs because all their electrochemical properties strongly depend on the preparation process that also determines the morphology of the nanostructure. Some properties of the MnO_2-based supercapacitors are also discussed in this context, and we direct the reader to the review [22] for more details.

Table 1. Summary of crystallographic data of some manganese dioxide (MDO) compounds.

Compound	Mineral	Crystal Symmetry	Lattice Parameters (Å)	Features
α-MnO_2	hollandite	tetragonal ($I4/m$)	a = 9.96; c = 2.85	(2 × 2) tunnel
R-MnO_2	ramsdellite	orthorhombic ($Pbnm$)	a = 4.53; b = 9.27; c = 2.87	(1 × 2) tunnel
β-MnO_2	pyrolusite	tetragonal ($P4_2/mnm$)	a = 4.39; c = 2.87	(1 × 1) tunnel
γ-MnO_2	nsutite	complex tunnel (hex.)	a = 9.65; c = 4.43	(1 × 1)/(1 × 2)
δ-MnO_2	birnessite	rhombohedral (R-3m)	a_{hex} = 2.94; c_{hex} = 21.86	(1 × ∞) layer
Mg-Bir	Mg-birnessite	monoclinic ($C2/m$)	a = 5.18; b = 2. 84; c = 7.33	(1 × ∞) layer
Na-Bir	Na-birnessite	monoclinic ($C2/m$)	a = 5.17; b = 2.85; c = 7.32	(1 × ∞) layer
ε-MnO_2	akhtenkite	hexagonal ($P63/mmc$)	a = 2.85; c = 4.65	dense stack
λ-MnO_2	spinel	cubic ($Fd3m$)	a = 8.04	(1 × 1) tunnel
ψ-MnO_2	psilomelane	monoclinic ($P2/m$)	a = 9.56; b = 2.88; c = 13.85	(2 × 3) tunnel
T-MnO_2	todorokite	monoclinic ($P2/m$)	a = 9.75; b = 2.85; c = 9.59	(3 × 3) tunnel

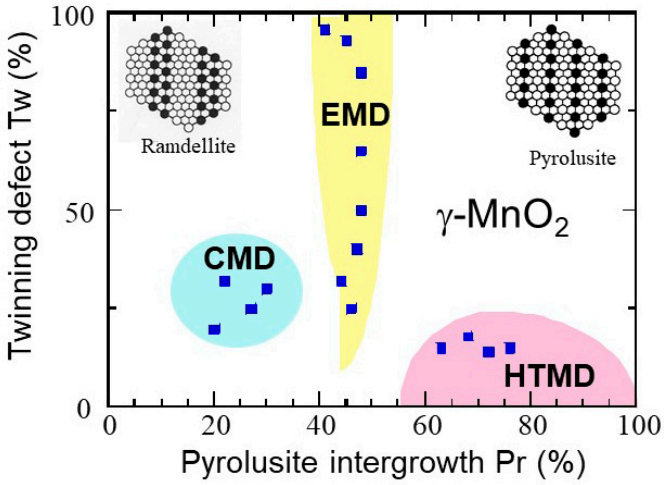

Figure 2. Degree of micro-twinnings as a function of the pyrolusite intergrowth in synthesized CMD, EMD, and HTMD manganese dioxides.

In this review article, we investigate the properties of MnO_2 nanomaterials with different morphologies. Their structural and physical properties are reported. Periodic (α-, β-, and R-MnO_2) and aperiodic (γ-MnO_2) structures are considered. In Section 2, we briefly discuss the beneficial effect of nanosizing. In Section 3, we summarize the techniques used for the synthesis of nanomaterials as the structure and morphology of MnO_2 are related to the synthesis conditions (reagents, temperature, pH, etc.). Section 4 is devoted to the electrochemical features of bulk MDOs. In the following Sections 5–8, we report the properties of the various nanostructures (nanourchins, doped MnO_2 nanomaterials, polypyrrole-coated MnO_2, nanocomposites). For each material, the effects of the morphology of nano MDOs on their physical and electrochemical performance are evidenced. Applications such as electrodes in lithium batteries and supercapacitors are examined.

2. Beneficial Effect of Nanosizing on Transport Properties

One major reason for the use of nanosized particles of materials for energy storage comes from their poor transport properties that imply poor rate performance of these electrochemical devices. This is the case for oxides used as electrodes in batteries and supercapacitors. For example, the electronic conductivity of MnO_2 is $\approx 10^{-8}$ S·cm^{-1} at room temperature, which requires some sophisticated technology such as the use of slurry containing carbon (carbon "Super P", acetylene black, rGO, CNTs, etc.) or deposition at the surface of the grains for enhanced charge carrier transport [23]. Achieving high rate capability depends ultimately on the geometry of the active objects building the positive (cathode) and negative (anode) electrodes. The performance of an electrode is governed by the transport of both electrons and ions; consequently, the ionic and electronic conductivity of the materials must be considered.

Let us examine the ionic and electronic transport properties of particles as a function of size L (Figure 3a). As the motion of ions is a diffusion process, the characteristic time τ for an ionic species i (in practice Li^+ ions in the present case) to reach the surface of any active particle of dimension L is given by the second Fick's law that applies the chemical diffusion coefficient with D^* of moving ions [2]. In the case when the chemical reaction proceeds by a single phase (*sp*) process, i.e., within a solid solution, τ is given by:

$$\tau_{sp} = \frac{L^2}{4\pi D^*}, \quad (1)$$

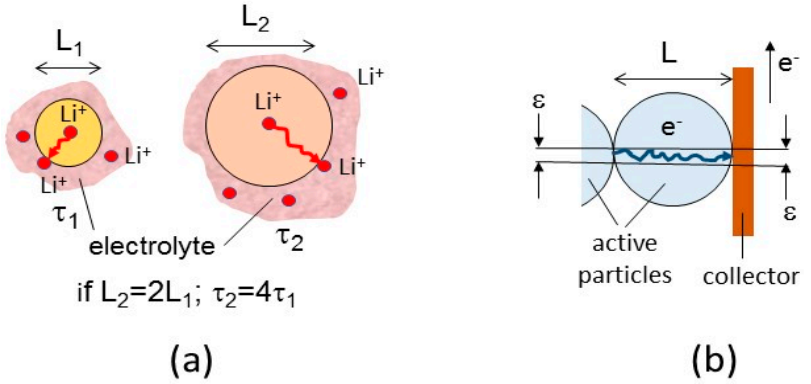

Figure 3. Schematic representation of the pathway for ions (**a**) and electrons (**b**) passing through particles of active electrode material.

In the case of a two-phase (*tp*) process, for which there is a separation between a Li-rich and Li-poor phase instead of a solid solution, the chemical reaction proceeds by nucleation of the phases and motion of the propagation of the boundaries that separate the two phases. In this case, the characteristic time is given by:

$$\tau_{tp} = \frac{F^2}{2V_m} \frac{L^2}{\langle \sigma^i \rangle \Delta\mu^i} \quad (2)$$

where V_m is the molar mass of the active compound, σ^i the ionic conductivity, and $\Delta\mu^i$ the difference of the chemical potential of ions between the two phases. Note that in both cases τ is proportional to L^2. Therefore, by reducing the size L of the active particles of electrodes from micrometer to nanometer, one reduces τ for the diffusion of ionic species in the solid-state phase by a factor of 10^6. A decrease of τ corresponds to a minimization of the charge duration of the battery. For example, let us consider the case of the Li_xMnO_2 electrode in which Li^+ ions are moving in the tunnel of an EMD framework. The chemical diffusion coefficient of the lithium in this case is $D^* = 3.4 \times 10^{-12}$ cm^2·s^{-1} at room temperature with an activation energy of 30 kJ [24], so that, at a fast rate of extraction of Li^+ ions from the host lattice, the charge is achieved in 27 h for a 10-µm particle size. However,

this time will be reduced to 4 min for a 500-nm particle size. Thus, 500-nm sized particles can be fully charged/discharged even at 4C rate (0.7 $A \cdot g^{-1}$). However, in addition to the effects of size and distribution of particles on the insertion reaction mechanism, the effect of the high specific surface area of nanoparticles (safety problems) and the minimization of the volume expansion upon Li-ion insertion should be considered.

The second transport parameter is the electronic conductivity σ_e of the particles, which monitors the rate capability of the electrode, i.e., overpotential. The electronic current flowing through a particle is a function of electron diffusivity expressed by the Einstein relation:

$$D_e = \frac{k_B T}{|e|} \mu_e, \tag{3}$$

where μ_e is the electron mobility, T the absolute temperature, k_B the Boltzmann constant, and $|e|$ the elementary charge. Let us consider the case of electrons flowing through one particle between the current collector and the neighboring one with a small contact area ε_c (Figure 3b). According to the ohmic law, the resistance of the particle R_e is given by

$$R_e = \frac{L}{\sigma_e \varepsilon_c} \tag{4}$$

Consequently, the resistance can be reduced by decreasing the particle size to increase the surface area of the material, provided that the whole surface area of the particles can be considered as the contact area with the collector. To reach approximately this goal, the MnO_2 particles can be coated with a conductive material [25,26]. This will be discussed in Sections 7 and 8.

3. Synthesis of MnO_2 Nanomaterials

Several routes are currently used for the synthesis of MnO_2: electrochemical methods [21,27,28] and eco-friendly wet-chemical [29,30] techniques have been reported. As already mentioned in the introduction, samples prepared by the electrochemical method lead to γ- and ε-MnO_2 and their synthesis has been reported in a recent review [20]. We thus focus attention in this section on the other synthesis routes. Various strategies have emerged as new methods to synthesize nanostructured MnO_2 samples with different controlled-morphologies (shape and size). The synthetic methods for nanostructured MnO_2 include simple reduction, coprecipitation, sol-gel, thermal decomposition, and the hydrothermal synthesis molten-salt method (see [31] for a review). Various nano-structured objects investigated over the years include nanowires [32–34], nanorods [35,36], nanoflowers [37], nanosheets [38], nanoflakes [39,40], nanotubes [41,42], nanourchins [43,44], nanospheres [45], nanobelts [46], nanodisks [47], and nanofibers [48]. The various morphologies of nanostructure MnO_2 materials are illustrated by the SEM images in Figure 4. On the basis of classical synthesis, MDOs are classically prepared by oxidation of aqueous Mn^{2+} solution using various oxidants such as MnO^{4-}, $S_2O_8{}^{2-}$, H_2O_2, O_3, ClO^{3-}, $Cr_2O_7{}^{2-}$, etc. It has been experimentally shown that the size and morphology of particles depend on the nature of the oxidant and the pH of the mixture. For example, the crystallization domains of the MnO_2 structures in the pH/synthesis temperature diagram are shown in Figure 5 [49]. In the following, we report the different routes used for the synthesis of nano-MnO_2 including examples of the literature.

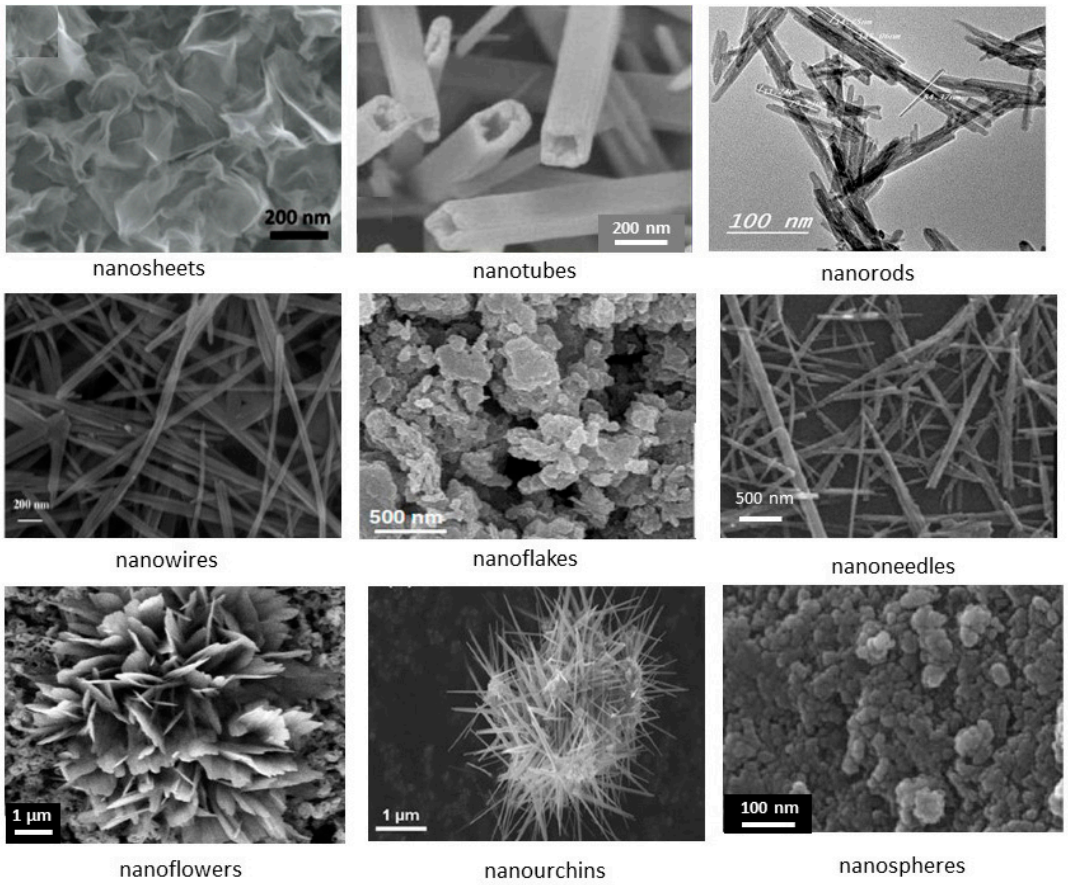

Figure 4. SEM images of the various nanostructured MnO_2 materials. These micrographs show the morphologies of the different MDO samples described in the text.

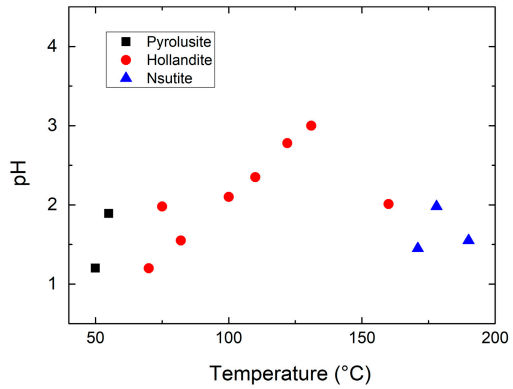

Figure 5. Growth regions of the MnO_2 structures in the pH/synthesis temperature diagram (from Ref. [49], unpublished).

3.1. Redox Reaction

Several processes, in which Mn^{7+} is reduce to Mn^{4+}, were used to grow α-MnO_2 nanocrystals. However, the preparation of polymorph MnO_2 from reactions of MnO_4^- and Mn^{2+} are known to be critical on the nature of precursors [50]. The most popular route consists of the reduction of $KMnO_4$ by salts or organic substances. As an example, with manganese acetate as oxidant of potassium permanganate, the simple redox reaction can be expressed by:

$$3Mn(CH_3COO)_2 + KMnO_4 + 2H_2O \rightarrow 5\,MnO_2 + 4CH_3COOH + 2CH_3COOK. \quad (5)$$

Ragupathy et al. [45] prepared MnO_2 nanospheres by reduction of $KMnO_4$ by aniline. The mole ratio of $KMnO_4$ to aniline was 2:1. The as-synthesized amorphous MnO_2 converts into crystalline α-form upon annealing at temperatures <400 °C. Hashem et al. synthesized two polymorph MnO_2 nanorods using redox reaction between $(NH_4)_2S_2O_8$ and $MnSO_4{\cdot}4H_2O$ for α-MnO_2 and $(NH_4)_2S_2O_8$ and $Mn(NO_3)_2{\cdot}4H_2O$ for β-MnO_2 [51]. Rod-shaped structures of α-MnO_2 and β-MnO_2 are shown in Figure 6. The diameters of these rods are in the range of 15–20 nm for α-MnO_2 and β-MnO_2 samples, respectively.

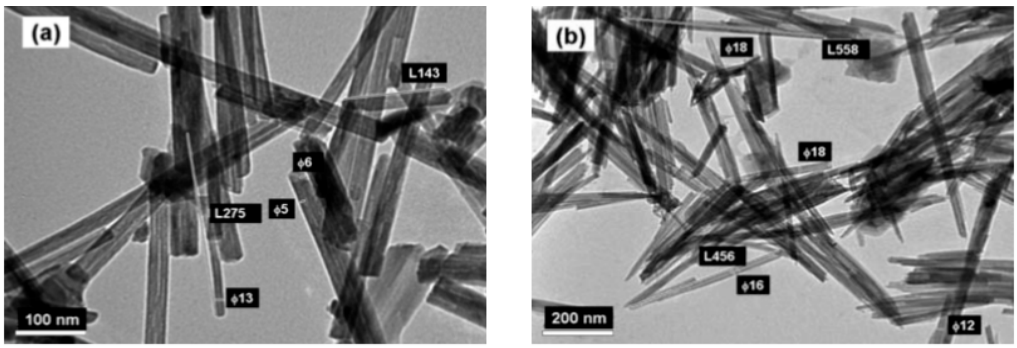

Figure 6. Transmission electron microscope (TEM) images of (**a**) α-MnO_2 and (**b**) β-MnO_2 nanorods prepared through redox reaction. Values of diameter and length of nanorods are in nanometers and preceded by the letters "*Φ*" and "*L*", respectively.

Single-crystalline α-MnO_2 nanorods were synthesized by a hydrothermal method based on the redox reactions between the permanganate anion MnO_4^- and H_2O in a mixture containing $KMnO_4$ and HNO_3 [52]. These results are consistent with the investigations of Yin et al. [53] who studied the effects of metal cations and protons on the structures and morphologies of MnO_2. K^+ and H^+ are competitive in solution to form: (i) cryptomelane α-MnO_2 is formed when the amount of K^+ is higher than the amount of H^+; (ii) for the growth of the pyrolusite structure β-MnO_2 occurs at a higher quantity of H^+; (iii) the layered phase δ-MnO_2 is obtained at a concentration of K^+ much greater than that of H^+. Liu et al. [54] successfully prepared nanosheets (typical thickness 1 nm) using a slow redox reaction between $KMnO_4$ and sodium dodecyl sulfate (SDS) in acidic medium (diluted H_2SO_4), in which SDS served as the precursor to reduce $KMnO_4$. Jeong and Manthiram [55] mentioned the preparation of MnO_2 by the reduction of $KMnO_4$ using various inorganic reducing agents such as potassium borohydride, sodium dithionate, and sodium hypophosphite. MnO_2 and Pb, Ni-mixed MnO_2 were prepared at room temperature by the reduction of $KMnO_4$ with Mn/Ni/Pb acetate solutions [56]. The solid-state reaction between Mn^{7+} and Mn^{2+} in high-energy ball milling was successfully applied to grow α-MnO_2 nanorods doped with different metal M^{2+} cations (M = Cu, Co, Ni, and Zn). The synthesized samples exhibited excellent textural characteristics, i.e., BET surface area of ~128 $m^2{\cdot}g^{-1}$ and pore size of ~8 nm [57].

3.2. Thermal Decomposition

Lee et al. prepared $K_xMnO_{2+\delta}{\cdot}nH_2O$ and amorphous MnO_2 materials by direct thermal decomposition of finely ground $KMnO_4$ powders at T in the range 350–100 °C which contained a large amorphous/crystalline ratio [58]. Komaba et al. [59] fabricated K_xMnO_2 powders (δ-structure, x = 24.7 wt %) synthesized by simple decomposition of $KMnO_4$ at 300–800 °C in air. Further washing in 1 $mol{\cdot}L^{-1}$ HCl aqueous solution reduced the potassium content to x = 0.26 wt %. Layered-type δ-MnO_2 nanoflake-like particles were prepared via the thermal decomposition of $KMnO_4$ according to the reaction:

$$5KMnO_4 \rightarrow K_3MnO_4 + K_2MnO_4 + 3MnO_2 + 3O_2, \quad (6)$$

The MDO sample was obtained after heating at 350 °C for 5 h [60].

3.3. Hydrothermal Route

The nature of the MDO nanomaterials formed by this method depends on temperature, fill level in the pressure vessel, and solvent. By simply tuning of the hydrothermal reaction time of the decomposition of $KMnO_4$ and $MnSO_4 \cdot H_2O$ in heated aqueous solution, Subramanian et al. [61] obtained different nanoarchitectures of MnO_2 particles by changing the hydrothermal time from 1 to 18 h. For the mixture heated at 140 °C for 1 h, they reported the formation of flowerlike nanowhiskers of MnO_2, which transformed to α-MnO_2 nanorods after 12 h. Xiao et al. [62] prepared three types of MnO_2 nanostructures: microsphere/nanosheet core–corona hierarchical architectures, one-dimensional (1D) nanorods, and nanotubes, employing a simple hydrothermal process in an autoclave heated at different temperatures (100–200 °C) for the same duration (12 h). In a typical synthesis, the hydrothermal decomposition of single $KMnO_4$ to produce the α-MnO_2 phase occurs in acidic conditions in the absence of templates or surfactants: concentrated H_2SO_4 or HCl (37 wt %) were added to deionized water [63]. The nanosized birnessite-type δ-MnO_2 (monoclinic, $C2/m$) was formed at 100 °C, while pure α-MnO_2 nanorods (tetragonal, $I4/m$) crystallized at 120 °C, transforming to α-MnO_2 1D nanotubes at 140 °C. Single-crystal β-MnO_2 nanotubes (200–500 nm diameters) were prepared by a simple hydrothermal method by oxidizing $MnSO_4$ with $NaClO_3$ in the presence of poly(vinyl pyrrolidone) (PVP) [42]. Wang et al. [63,64] synthesized various nanostructured MnO_2 polymorphs (α-, β-, γ-, and δ-forms) using a common hydrothermal method with pH and NH_4^+ cation concentration adjustment. All nano-samples have a similar formation of layered δ-MnO_2. β- and γ-MnO_2 grown as nanowires/nanorods (Figure 7), while α-MnO_2 and todorokite-type MnO_2 have fiber or needle morphologies [43]. Well-crystallized nanorods of α-MnO_2 (12 nm diameter) were prepared by the hydrothermal route in the presence of poly(sodium 4-styrene-sulfonate) using $KMnO_4$ and $MnSO_4$ mixed in a solution of water and ethanol (4:1 in volume) [65]. A polyethylene glycol (PEG) polymer-precursor route was employed to prepare γ-MnO_2 nanowires/nanotubes. In a typical synthesis, $MnSO_4$ aqueous solution was mixed with PEG-6000 dissolved in aqueous methanol solution forming the precursor to which NaOH was added. The nanotubes were obtained after treatment in an autoclave at 120 °C for 20 h [66]. Ma et al. [67] synthesized layered MnO_2 nanobelts by the hydrothermal treatment of Mn_2O_3 powders in an aqueous solution of NaOH at 170 °C for >72 h. The structure of nanobelts is characterized by a basal spacing of ~7.1 Å indicating the transformation of Mn_2O_3 to δ-MnO_2.

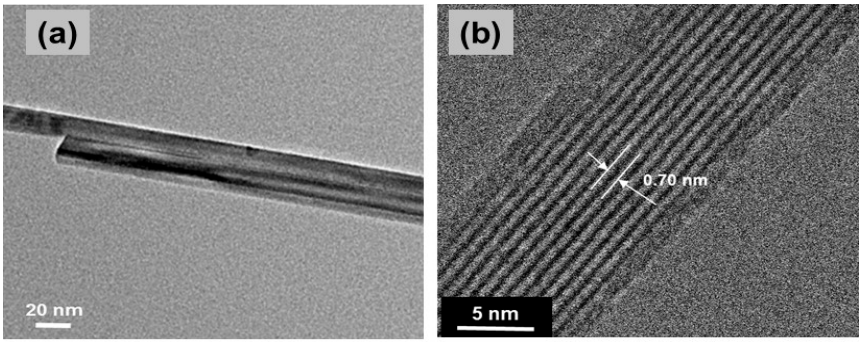

Figure 7. High-resolution transmission electron microscope (HRTEM) images of α-MnO_2 nanowires grown by the hydrothermal route. The inter-layer space ~0.7 nm corresponds to the (110) plane of α-MnO_2. Reproduced with permission from [43]. Springer, 2016.

Cheng et al. [68] synthesized α-MnO_2 nanowires on the basis of the hydrothermal reaction between $KMnO_4$ and $MnSO_4 \cdot H_2O$ in aqueous solution at 140 °C for 12 h, and γ-MnO_2 nanowires from the mixture of $MnSO_4$ and $(NH_4)_2S_2O_8$ treated at 90 °C for 24 h. Cryptomelane-type manganese dioxide (α-K_xMnO_2) nanofibers with typical diameters of 20–60 nm and lengths of 1–6 μm were grown by reacting $KMnO_4$ with $MnSO_4$ under hydrothermal conditions (140 °C for 12 h) [69]. The nanofibers

crystallize in a body centered tetragonal structure (space group $I4/m$) with unit cell parameters a = 9.8241(5) Å and c = 2.8523(1) Å. Their actual composition is $K_{0.11}MnO_{2.07}$.

3.4. Refluxing Route

The refluxing method allows in situ sample crystallization and requires ambient conditions of atmospheric pressure and temperature below the boiling point of solvent. This method requires heating a solution with an attached condenser preventing loss of reagents. However, many organic compounds have low boiling points and will vaporize upon exposure to such high heat [70]. Reflux treatment is convenient for large-scale preparation. The one-step direct refluxing route to synthesize α-MnO_2 consists of the reduction of $KMnO_4$, $NaCr_2O_7$ or $KClO_3$ using inorganic or organic acid as additive [71]. Wang et al. [72] prepared λ-MnO_2 nanodisks by the refluxing technique using $Mn(Ac)_2{\cdot}4H_2O$ and polyvinyl pyrrolidone (PVP) in dimethyl sulfoxide (DMSO) solution. The success of this synthesis is due to the synergic control of the surfactant (PVP) and the solvent (DMSO) that promote MnO_2 nanoparticles. A reflux treatment of $KMnO_4$ and $MnSO_4$ in HNO_3 acidic solution was used to synthesize single-crystalline β-MnO_2 nanorods. Cui et al. [36] reported that the dimensions depend on the acidity of the solution: nanorods exhibited diameters of 20–50 nm and lengths that ranged from approximately 0.5 to 2.0 μm with decreasing HNO_3 concentrations from 0.8 to 0.1 mol·L^{-1}. Cryptomelane-type α-MnO_2 nanofibers with particle sizes as small as 6 nm were synthesized on the basis of the reduction of $KMnO_4$ by H_2O_2 under acidic conditions followed by reflux. The particle size and crystallite size were adjusted by varying the pH of the mixture using an acetate-containing buffer solution and HNO_3 [73].

3.5. Catalytic Reaction

A homogeneous catalyst can reduce the potential energy of a chemical reaction (for example, oxidation of $MnSO_4$) and control the growth of oxide materials [74]. The synthesis of birnessite-type MnO_2 electrode for supercapacitors was realized by in situ electrochemical oxidation of Mn_3O_4 films composed of nanowall arrays with porous structure [75]. The preparation of a core-shell structure (α- and β-MnO_2 forms) with spherically aligned nanorods by a simple room-temperature solution-based catalytic reaction using $AgNO_3$ was reported. The catalyst dissolved in aqueous solution was added to the aqueous solution of $MnSO_4{\cdot}H_2O$ and $(NH_4)_2S_2O_8$ with concentrated sulfuric acid (98%). A suitable amount of acid promoted the formation of intermediate Mn^{3+} that disproportionated to α-MnO_2 and Mn^{2+} [76].

3.6. Sol-Gel Route

In this method, the gel is generated through a redox reaction between $KMnO_4$ and a carboxylic acid, i.e., citric, tartaric, fumaric acid, etc. [44]. The formation of MnO_2 tunnel structures is known to be controlled by adjustment of the pH, with H_3O^+ and/or H_2O [77,78]: the growth of α-MnO_2 is favored in aqueous concentrated acid [72], whereas δ-MnO_2 is formed in aqueous concentrated base [73]. Oxidation of Mn^{2+} cations (in $MnSO_4$) by $S_2O_8{}^{2-}$ anions (in $(NH_4)_2S_2O_8$) in aqueous solution without catalysts is achieved according the chemical reaction:

$$MnSO_4 + (NH_4)_2S_2O_8) + 2H_2O \rightarrow MnO_2 + (NH_4)_2S_2O_4 + 2H_2SO_4 \quad (7)$$

Nanowires are obtained by this technique [32]. An alternative method uses manganese sulfate $MnSO_4$ and potassium peroxodisulfate $K_2S_2O_8$ as starting materials [79]. Oaki and Imai [80] prepared δ-MnO_2 nanosheets (10 nm thick) using a sol-gel method assisted by ethylene diamine tetra-acetate (EDTA) as chelating agent. The reaction started upon mixing solutions containing Mn^{2+}/EDTA and NaOH (basic solution). A low-temperature sol-gel process using manganese acetate tetra-hydrate $(CH_3COO)_2Mn{\cdot}4H_2O$ and concentrated nitric acid (67 wt %) associated with different surfactants in ethanol solvent was applied. MnO_2 nanowires and nanorods were formed with the assistance of

cetyltrimethyl ammonium bromide and polyvinyl pyrrolidone, respectively [81]. Figure 8 shows the typical X-ray diffraction pattern of the α-K_xMnO_2 structure synthesized by the sol-gel route [43].

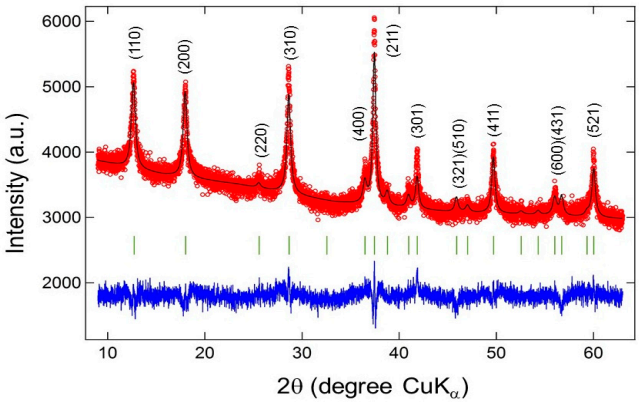

Figure 8. Typical X-ray diffraction pattern of nanostructured α-K_xMnO_2 ($x < 0.1$) synthesized by the sol-gel route. Reproduced with permission from [43]. Springer, 2016.

3.7. Co-Precipitation Method

This technique, which offers advantages such as simple and rapid preparative synthesis, as well as easy control of particle size and composition can be achieved without surfactant. Currently, the co-precipitation process is performed by using manganese salts with two different anions in equal concentration, such as manganese(II) sulfate and manganese oxalate for example. The pH must be adjusted to 12 by addition of NaOH to obtain brown precipitates that are MnO_2 precursors [82]. Nanoneedles were obtained using $MnCl_2$ mixed with isopropanol heated at ≈80 °C in a refluxing process and $KMnO_4$ dissolved in distilled water [83]. A simple co-precipitation of MnO_2 was achieved by mixing aqueous solutions of $KMnO_4$ and ($MnSO_4 \cdot H_2O$), where $KMn^{VII}O_4$ is used as the oxidizing agent for $Mn^{II}SO_4$ in distilled water [84]. The $KMnO_4$:($MnSO_4 \cdot H_2O$) molar ratio of 2:3 leads to a dark brown precipitate with the final chemical formula $K_{0.02}MnO_2H_{0.33} \cdot 0.53H_2O$ [85].

Nanostructured α-$MnO_2 \cdot nH_2O$ (BET = 303 $m^2 \cdot g^{-1}$) obtained by precipitation of $KMnO_4$ and Mn(II) acetate in aqueous solutions was also reported [86]. MnO_2 nanosheets used as artificial enzymes (nano-oxidases) were obtained by exfoliation of bulk material prepared by precipitation of $MnCl_2 \cdot 4H_2O$ and a mixture of tetramethylammonium hydroxide (TMA·OH) and H_2O_2 in aqueous solution [8]. α-MnO_2 nanosheets were also formed by co-precipitation of $MnCl_2 \cdot 4H_2O$ and $MnC_2O_4 \cdot 2H_2O$ in aqueous solution with addition of sodium hydroxide to control the pH of the solution [87]. Hydrothermal synthesis was applied to grow two types of MnO_2 nanorods: (i) rutile-type β-MnO_2 due to a redox reaction (135 °C for 12 h) between manganese(II) sulfate with ammonium persulfate and (ii) hollandite-type α-K_xMnO_2 (x = 0.15 and 0.18) due to the decomposition of potassium permanganate obtained in the presence of sulfuric acid added to water after stirring to form a solution (150 °C for 8 h) [88]. The EPR spectra of α-K_xMnO_2 nanorods contain two signals. One is attributed to Mn^{4+}; the other one to manganese in mixed-valence Mn^{4+}/Mn^{3+} environment close to K^+ ions [89]. Urchin-like α-MnO_2 materials were also prepared through a simple precipitation reaction of H_2SO_4 and $KMnO_4$ in aqueous solution heated at 85 °C [90]. A two-step green precipitation route was used for the reduction of $KMnO_4$ in the presence of natural extracts such as extracts of grape stems and apple peels to initiate the nucleation process [91]. TEM images showed the presence of short and long nanorods with diameters in the range 28–70 nm and lengths in the range 85–180 nm, which form dense agglomerates. Another green synthesis pathway consists of the mixture of manganese acetate salt as precursor and methanolic extract of *phyllanthus amarus* plant as reducing agent stabilized by curcumin extracted from turmeric [92].

3.8. Oxidation Reaction in Alkaline Conditions

Jana et al. [93] reported the fast synthesis of rod-shaped MnO_2 nanoparticles by the reaction between $MnCl_2{\cdot}4H_2O$ and sodium dodecylbenzene sulfonate $NaC_{18}H_{29}SO_3$ at room temperature in aqueous solution in alkaline conditions adding NaOH solution. The MnO_2 nanorods and nanospherical particles were grown from variable surfactant concentrations. These nanorods had additional reaction in an aqueous solution of $AgNO_3$ to become Ag-doped MnO_2 nanoflowers [37]. Song et al. [44] fabricated urchin-like α-MnO_2 by the reaction of $MnSO_4$ and $KClO_3$ using the sodium dodecyl sulfate (SDS)-assisted hydrothermal route.

3.9. Oxidation Reaction in Acidic Conditions

α-K_xMnO_2 was prepared using potassium permanganate $KMnO_4$ under acid conditions dissolved in distilled water with various acids, for example, hydrochloric acid solution [41]. Kijima et al. [77] synthesized nanoparticles of α- and γ-MnO_2 by an ozone-oxidation method in acidic medium. The α-MnO_2 phase was produced at high H_2SO_4 concentrations and high reaction temperatures using three pairs of manganese-salt-hydrates and acid, i.e., $MnSO_4{\cdot}5H_2O$ and H_2SO_4, $Mn(NO_3)_2{\cdot}6H_2O$ and HNO_3, $MnCl_2{\cdot}4H_2O$ and HCl. In contrast, the γ-MnO_2 phase was obtained by the ozone-oxidation of $MnSO_4$ dissolved in lower H_2SO_4 concentrations at lower temperatures, again followed by ozone oxidations of $Mn(NO_3)_2$ dissolved in HNO_3 or $MnCl_2$ dissolved in HCl.

3.10. Molten Salt Method

Nanowires MnO_2 were formed using KNO_3 as molten salt with $NaNO_3$ and $LiNO_3$ applied as the reaction media. [94]. Large scale synthesis of 1D α/β-MnO_2 nanowires was realized by mixing anhydrous $MnSO_4$ and KNO_3 heated at 380 °C for 3 h, loading of the $KNO_3/MnSO_4$ weight ratio of 15. Similar procedure was used for the synthesis of β-MnO_2 with a mixture of $NaNO_3$ and $LiNO_3$-added $MnSO_4$. The formation mechanism of α/β-MnO_2 nanostructures was proposed on the basis of the time-dependent experiments due to the kinetics of inserted cations into the tunnel structures: larger cations K^+ in the (2×2) cavities of α-MnO_2 versus smaller cations Li^+ or Na^+ in the (1×1) cavities of β-MnO_2 [94].

3.11. Witzrmann's Method

This consists of the reaction between $KMnO_4$ and small saccharides, i.e., glucose and sucrose or other polyalcohols in non-aqueous sol-gel chemistry (alcoholic solution). Ching et al. developed a modified sol-gel reaction between tetra-alkyl ammonium permanganate and methanol. MnO_2 nanopowders were well crystallized after a calcination at 450 °C for 2 h [95].

3.12. Template Approach

Aerogel MnO_2 with ultralow density (~0.5 $mg{\cdot}cm^{-3}$) was prepared from nanosheet colloids via an ice-template method for use as an effective absorbent for toxic reducing gas [96].

4. Electrochemistry of Li-MDOs

The various forms of MnO_2 have been intensively studied as electrode materials of primary zinc-alkaline cells, primary lithium cells in aqueous electrolytes, rechargeable lithium batteries, and electrodes of asymmetric supercapacitors. In addition to the interest of the various structures and specific properties of the tunnel framework, these materials possess the advantages of low cost, sufficiently high specific capacitance, and environmentally friendly nature. At the end of this Section, we briefly examine the electrochemical response of some MDO phases in batteries and their properties as supercapacitor electrodes.

The "energy density" is a common measure in evaluating battery systems. Specific energy stored (in Wh·kg^{-1}) in a battery is measured by discharging a battery at an appropriate current:

$$E_{pr} = V_{oc}\, Q_{dis}, \tag{8}$$

where V_{oc} is the operating potential in volt (V) obtained from the energy change for the cell reaction and Q_{th} is the specific capacity in ampere-hour per mass (Ah·kg^{-1}), or equivalently in mAh·g^{-1}. Its theoretical value is obtained from the Faraday law [1]:

$$Q_{th} = \frac{1000 \times nF}{3600 \times M_w} = \frac{26.8}{M_w} \times n, \tag{9}$$

where M_w is the molecular mass of the "limiting" electrode material. With the transfer of 1e$^-$ per formula unit, the theoretical specific capacity of MnO_2 (M_w = 92.93 g·mol^{-1}) is 308 mAh·g^{-1}.

The three forms of synthesized MnO_2 (EMD, CMD, and HTMD) considered as excellent cathode materials for zinc-alkaline cells, have a hexagonally close-packed structure closely related to the polymorphs β- and γ-MnO_2 structures. Chabre and Pannetier [9] showed that the electrochemical features of γ-MnO_2 are strongly influenced by the irregular intergrowth of pyrolysite in the ramsdellite framework creating micro-twinnings and De Wolff defects. Using Raman spectroscopy, Julien et al. [97] quantitatively elucidated the structural disorder present in γ-MnO_2. It was found that the usual range of pyrolysite intergrowth, Pr, depends on the synthesis. CMD is currently close to ramsdellite with Pr < 40%, EMD has a structure with 40% < Pr < 60% and HTMD is close to pyrolusite (see Figure 2). Due to their superior structural and electrochemical performances, EMD compounds prepared by electrolysis of an acidic slurry of ground MnO_2 ore at ~95 °C are widely used in the power source industry [66,98]. McBreen [99] reported that the electrochemistry of β-MnO_2 in 7 mol·L^{-1} KOH alkaline electrolyte differs from γ-MnO_2 showing no lattice dilatation, while the relationship between synthesis conditions and the performances of CMDs and HTMDs was established by Sarciaux et al. [100]. It appears that the maximum reversible Li uptake depends strongly on concentration of Pr and Mt defects. The largest reversible intercalation capacities are obtained from γ-MnO_2 with low Pr and Mt values. For HTMD sample with Pr = 45% and Mt = 8%, ~0.9Li/Mn can be inserted in the potential range 2–4 V at $C/6$ rate. Malankar et al. [101] reported the discharge characteristics of γ-MnO_2 with De Wolff disorder in the range 0.21 < Pr < 0.32 in alkaline medium. At low discharge rate, two electrochemical steps govern the reduction of MnO_2: (i) the homogeneous phase reduction $MnO_2 \rightarrow MnO_{1.5}$ and (ii) the conversion of MnO_2 to MnOOH due to the increase of the concentration of Mn^{3+} and OH^- with the liberation of 1e$^-$. The discharge performances of nanostructured α-, β- and γ-MnO_2 were tested in alkaline Zn-MnO_2 cells using electrodes made of 85% active material, 10% acetylene black, and 5% PTFE; these cells deliver a discharge capacity of 235, 140, and 267 mAh·g^{-1} to an end potential of 0.8 V at constant current of 40 mA·g^{-1}, respectively [63].

The commercial DURACELL® alkaline MN1500 (cylindrical "AA" size), nominal voltage 1.5 V, lasts 140 h with a load of 32 Ω (constant current of 20 mA), which is reduced to ~8 h with a 3.9 Ω loading at higher current of 275 mA (capacity of 2200 mAh). The reactions of discharge are a reduction of the oxygen-rich MnO_2 and the oxidation of the zinc, while the transport of ions occurs through the conductive alkaline electrolyte according the simplified cell reaction:

$$Zn + 2MnO_2 \rightarrow ZnO + Mn_2O_3, \tag{10}$$

where the cathode is a mixture of EMD and graphite, while the anode is composed of high purity Zn powder held by a synthetic gel providing an open-circuit voltage (OCV) = 1.6 V [102]. Cheng et al. [66] improved the commercial AA (LR6)-type Zn-MnO_2 cells using nanostructured (nanowires/nanotubes) γ-MnO_2 synthesized via a polymer (polyethylene glycol, PEG) route. Figure 9a compares the voltage profiles for the modified and the commercial (Duracell MN1600) cells discharged at current of 0.1 A. The modified alkaline cell exhibits a similar discharge shape but delivers a significantly higher capacity

of 3.0 Ah against 2.3 Ah for the commercial battery. Extensive works on MnO_2 materials for both batteries and supercapacitors in aqueous solutions can be found in Refs. [98,103–110].

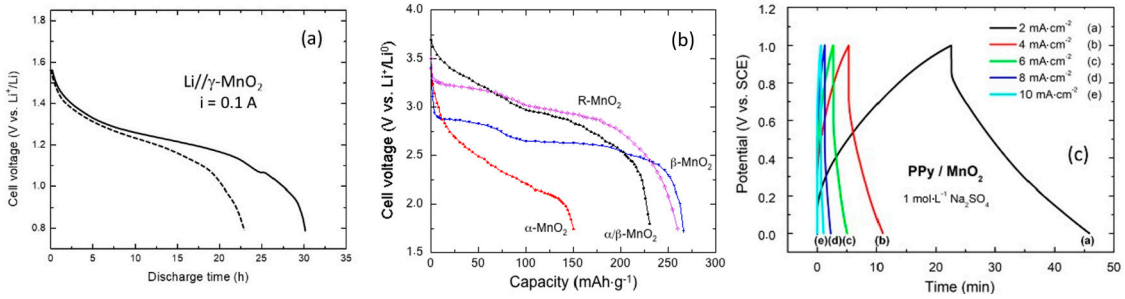

Figure 9. (**a**) Discharge profile of γ-MnO_2//Zn alkaline cells: laboratory cell made with γ-MnO_2 nanowires/nanotubes (solid line), and commercial battery Duracell MN1600 (dashed line). Reproduced with permission from [66]. Wiley, 2005; (**b**) Discharge curves lithium cells including single-phase α-MnO_2, β-MnO_2, R-MnO_2, and the stabilized phase α/β-MnO_2 as cathode. Reproduced with permission from Ref. [1]. Springer, 2016; (**c**) charge-discharge curves of α-MnO_2 in aqueous supercapacitors Reproduced with permission from [110]. Elsevier, 2013.

Due to their basic tetragonal structure formed by double (2 × 2) and (1 × 1) tunnels, cryptomelane and hollandite (α-MnO_2 polymorph) have shown possible applications as cathode materials for rechargeable Li-MnO_2 cells. Cheng et al. [68] compared the discharge features of α-MnO_2 nanowires with that of γ-MnO_2 nanorods and concluded that this latter cathode exhibits better electrochemical performance than the former one, i.e., 220 vs. 204 mAh·g^{-1} with the same conditions. The hollandite-type MnO_2 (HMDO) synthesized by reaction of $MnSO_4$ in concentrated H_2SO_4 in the presence of bubbling O_2 and ozone blended gas (50% in volume) was formed of coral-like particles and delivered a specific capacity of 165 mAh·g^{-1} after 20 cycles in the potential range 1.8–4.0 V [106]. Ma et al. [67] carried out electrochemical measurements on δ-MnO_2 nanobelts prepared by the hydrothermal method that reversibly hosted lithium as cathode in the potential range 1.0–4.8 V vs. Li^+/Li. Specific capacity of 220 mAh·g^{-1} was delivered over 45 cycles (uptake of 1.3 Li per formula unit) at current density of 20 mA·g^{-1}.

The discharge curves of different forms of manganese dioxide in Li-MnO_2 batteries, i.e., single-phase α-MnO_2, β-MnO_2, R-MnO_2, and the stabilized phase α/β-MnO_2 are shown in Figure 9b [1]. These results were obtained with cells using lithium counter-electrode, same electrolyte (1 mol·L^{-1} $LiPF_6$ in ethylenecarbonate (EC)/dimethylcarbonate (DMC) 1:1) and the same separator (Whatmann®-GF/D 70 mm Ø, Darmstadt, Germany), to make possible quantitative comparison. These data show that the stabilized two-phase α/β-MnO_2 sample delivers higher discharge capacity than the single-phase α-MnO_2. Furthermore, ramsdellite (R-MnO_2) and pyrolusite (β-MnO_2) display the highest discharge capacities. These materials present flat discharge curves while the hollandite structure shows an "S"-shaped discharge curve. On the initial discharge process the stabilized α/β-MnO_2 material delivers a specific capacity of 230 mAh·g^{-1}. This electrode shows good rechargeability with a capacity retention of 150 mAh·g^{-1} after 20 cycles. The initial capacity loss of 33% suggests that about 0.3 mol of inserted lithium ions are used [87]. Thackeray et al. [107] indicate that the rechargeability of R-MnO_2 is poor for the electrode cycled on deep discharge. The initial capacity 230 mAh·g^{-1} declines to 115 mAh·g^{-1} after 10 cycles at a current of 0.4 mA. This capacity loss is concomitant to structural changes upon the deep discharge process, i.e., large variations of the unit cell volume.

Several doping methods have been tested to improve the performance of MnO_2 in lithium cells. The Bi-doped MnO_2 was investigated by Bach et al. [108] suggesting that due to the presence of interlayer Bi^{3+} ions, a pillaring effect minimizes the structural modifications. Other examples of doping are treated in the following. Yang et al. [109] compared two commercial MnO_2 grades, i.e., EMD and CMD to hydrothermally synthesize α-MnO_2 composed of nanorods ~20 nm diameter in lithium cells.

The results demonstrated that, at a discharge current 50 $mA \cdot g^{-1}$, α-MnO_2 material delivers a specific capacity of 189 $mAh \cdot g^{-1}$ against 134 and 148 $mAh \cdot g^{-1}$ for, CMD and EMD type, respectively. Despite the favorable tunnel structure of γ-MnO_2, this phenomenon can be well understood in terms of the shortened diffusion path for Li^+ ions in low dimensional α-MnO_2.

The charge storage mechanism in a MnO_2 electrode for a supercapacitor performed in aqueous electrolyte has been described with two mechanisms [14]. The first one involves the insertion of alkali ions (Na^+, K^+ or Li^+) or protons (H^+) in the empty sites of the MnO_2 bulk upon the reduction reaction:

$$MnO_2 + H^+ + e^- \leftrightarrow MnOOH, \quad (11)$$

or

$$MnO_2 + Li^+ + e^- \leftrightarrow MnOOLi. \quad (12)$$

The second mechanism consists of adsorption of electrolyte cations (Li^+) on the surface of MnO_2

$$(MnO_2)_{surface} + Li^+ + e^- \leftrightarrow (MnO_2{}^-Li^+)_{surface}. \quad (13)$$

Typical galvanostatic charge-discharge profiles at various current densities (from 2 to 10 $mA \cdot cm^{-2}$) of an asymmetric supercapacitor using polypyrrole (PPy)/MnO_2 composite material in 1 $mol \cdot L^{-1}$ Na_2SO_4 aqueous solution as electrolyte are shown in Figure 9c [110]. The pseudo capacitance is attributed to the Mn^{4+}/Mn^{3+} reversible redox process accompanied by the insertion/deinsertion of alkali Na^+ cation or H_3O^+ protons from the electrolyte. A thin layer of PPy electrodeposited for 40 min on 250-nm sized γ-MnO_2 particles provide an energy density of 12.6 $Wh \cdot kg^{-1}$ and a power density of 34 $W \cdot g^{-1}$ [110].

5. MnO_2 Nanostructures: Example of Nanourchins

As we shall see in this section, urchin morphology was reported to be the best choice for enhanced electrochemical properties, so we have chosen it as an example. Recently, the synthesis process to grow MnO_2 nanoneedles (NNs) forming nanourchin (NUs) architecture has been investigated by different groups [30,45,46,88]. As shown above, many factors like acidity of the solution, cationic species (nature and concentration), and additive metal ions (Co^{2+}, Ni^{2+}, Fe^{3+}, Al^{3+}, etc.) greatly influence both the structure and the morphology of nanoparticles. For example, γ-MnO_2 urchin-like nanostructures are grown using Mn_3O_4 powder as raw material in H_2SO_4 solution; α-MnO_2 urchin-like composed of single nanorods are obtained from $KMnO_4$ and H_2SO_4 or from $MnSO_4 \cdot H_2O$, $K_2S_2O_8$ and concentrated sulfuric acid. A redox reaction between $MnSO_4$ and $(NH_4)_2S_2O_8$ as an oxidizing agent can also be used [97–117]. Details of the synthesis of urchin-like α-MnO_2 are shown schematically in Figure 10. Using two identical procedure, i.e., oxidation of $MnSO_4 \cdot H_2O$ by $K_2S_2O_8$, Zhang et al. [118] obtained two different phases that are γ-MnO_2 nanoparticles when using neutral (pH ~8) conditions, while α-MnO_2 NUs were grown in acidic (pH ~1) conditions with small addition of H_2SO_4. Wang et al. [119] synthesized sea urchin-like α-MnO_2 particles by a one-step chemistry route at room temperature using $MnSO_4$ in combination with KIO_4 as oxidant. Results revealed a product with lattice constants a = 9.840 Å and c = 2.856 Å ($I4/m$ space group) and a Brunauer-Emmett-Teller (BET) surface area of 201 $m^2 \cdot g^{-1}$.

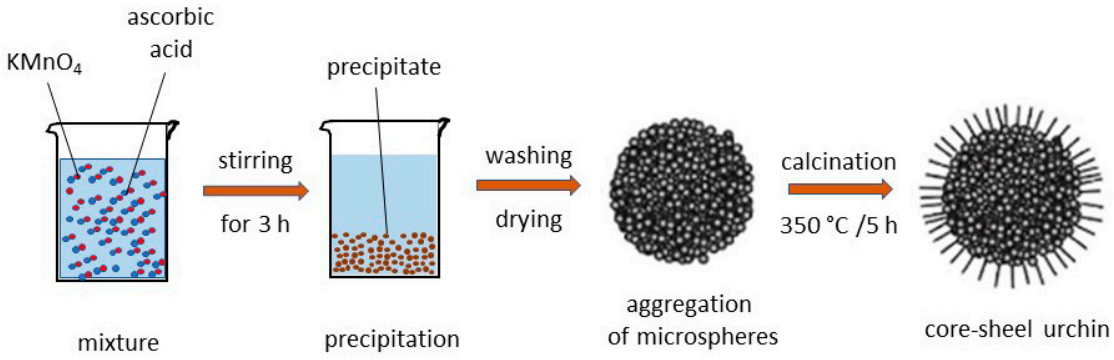

Figure 10. Schematic representation of the synthesis process of α-MnO_2 urchin-like structures.

Addition of Al^{3+} affects the hydrothermal synthesis of MnO_2 by modifying the chemical potential of the solution. Wang et al. [64] studied the synthesis conditions of various nanostructured MnO_2 polymorphs by tuning the pH and NH_4^+ cation concentration. It has been shown that NUs are generally synthesized by sol-gel methods in acidic medium that can control the morphology of the nanoparticles by direct redox reaction [43]. The choice of the cation species (K^+, NH_4^+, H^+) also plays a role evidenced in the hydrothermal crystallization [120]. For example, Yu et al. [30] fabricated various MnO_2 nanoneedles structures by redox reaction of $K_2S_2O_8$ and $MnSO_4{\cdot}H_2O$ with a concentrated sulfuric acid solution. The precipitate dried at 60 °C for 8 h is an urchins-shaped α-MnO_2 composed of nanorods with tetragonal lattice constants a = 9.826 Å, c = 2.854 Å. Using the same procedure with addition of $Fe(NO_3)_3{\cdot}9H_2O$ or $Al(NO_3)_3{\cdot}9H_2O$, a 3D clew-like ε-MnO_2 nanoarchitecture with hexagonal lattice constants of a = 2.846 Å, c = 3.530 Å was grown. In contrast, Li et al. [121] claimed the need of Ag^+ ion (via $AgNO_3$ solution) as catalyst agent for the crystallization of α-MnO_2 core-shell urchin-like structures. Urchin-like α-MnO_2 nanomaterials were also prepared without template or surfactant by a simple precipitation reaction of H_2SO_4 and $KMnO_4$ in aqueous solution [89]. Urchins are composed of aggregated crystalline nanorods with a mean diameter of 10 nm and a length of 200 nm. Chen et al. [90] suggested the formation mechanism of urchin-shaped α-MnO_2 from analysis of intermediates products formed in the hydrothermal process at different conditions of temperature and time ($55 < T < 85$ °C, 10 min $\leq t \leq$ 12 h). For T = 55 °C, t = 10 min, microspheres with diameter of 1 μm that consist of nanorods are formed; for T = 65 °C, t = 10 min, nanorods are epitaxially grown; for T = 75 °C, t = 10 min, the morphology turned into flower-shaped α-MnO_2; finally, at T = 85 °C the microspheres transform to urchin-like α-MnO_2. This suggests that the nanomaterial morphology is very sensitive to the temperature of the hydrothermal reaction. The synthesis of MnO_2 nanostructures with sea-urchin shapes carried out by a sodium dodecyl-sulfate (SDS)-assisted hydrothermal process was optimized by tuning the reaction time t while maintaining a constant temperature T = 150 °C. The products were composed of aggregated particles for t = 4 h, while the urchin-like morphology was well nucleated at t > 8 h. It was also shown that for low SDS concentration the nanostructure has a loose center [44].

NNs were prepared by a redox reaction of $KMnO_4$ and ascorbic acid. After stirring for 3 h, the precipitate dried at 100 °C for overnight aggregated with an urchin-like morphology (see Figure 11) [43]. These NNs grew in the tetragonal K_xMnO_2 structure with lattice parameters a = 9.8314(4) Å, c = 2.8586(1) Å and V = 276.31 Å^3. The mean crystallite size of the K_xMnO_2 nanoneedles was L_c = 14 nm. From both Rietveld refinement and elemental analysis, the K/Mn atomic ratio of ≈4% was evaluated. Generally, the presence of K^+ ions in the (2 × 2) tunnels of the hollandite lattice has an impeding effect for the chemical diffusion of the Li^+ ions. This is due to the much bigger ionic radius of K^+ (r = 1.33 Å) than Li^+ (r = 0.69 Å), which prevents the facile lithium motion in the MnO_2 framework [122].

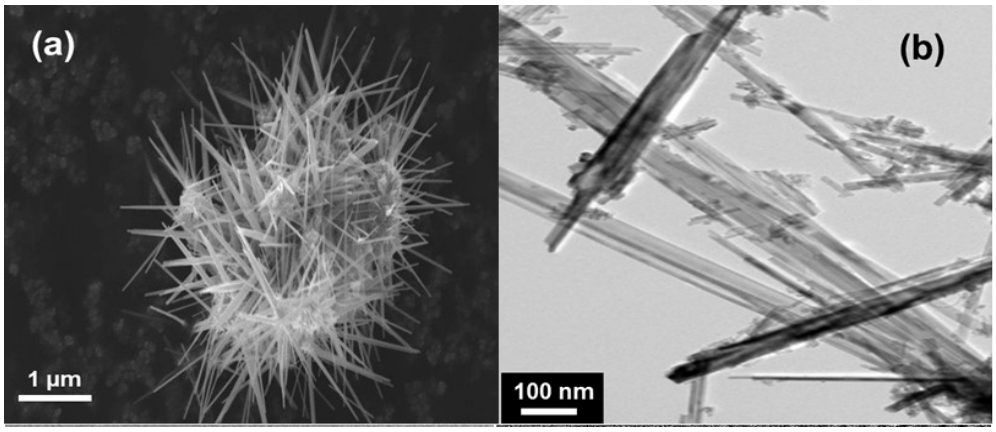

Figure 11. TEM images of urchin-shaped α-MnO_2 nanoarchitecture (**a**) and magnification of individual nanoneedles (**b**). Reproduced with permission from [43]. Springer, 2016.

The local structure of $K_{0.04}MnO_2$ nanoneedles was carefully analyzed by Raman and FTIR spectroscopy and magnetic measurements. Figure 12 shows the plot of the reciprocal magnetic susceptibility H/M vs. absolute temperature of MnO_2 nanoneedles (with H = magnetic field, M = magnetic moment). For $T > 150$ K, the magnetization M is linear in field H, so that the magnetic susceptibility χ_m is defined unambiguously by $\chi_m = M/H$ for NNs samples. The linear behavior of H/M up to 350 °C follows the Curie-Weiss law. This result evidences the strong antiferromagnetic interactions between the Mn moments as $\theta_p = -215$ K. The experimental value of the effective magnetic moment ($\mu_{eff} = 3.94\ \mu_B$) is slightly larger than that of Mn^{4+} ions ($\mu_{eff}(Mn^{4+}) = 3.87\ \mu_B$), which gives evidence of the presence of Mn^{3+} ions in the high spin state ($\mu_{eff}(Mn^{3+}) = 4.90\ \mu_B$). Thus, the concentration of Mn^{3+} ions is calculated [43] to be 5.8%. As it is actually larger than the residual concentration of K^+ ions, the local electrostatic charge neutrality imposes that oxygen vacancies should be responsible for the extra Mn^{3+} ions in the matrix; thus, the nanoneedle chemical formula is $K_{0.04}MnO_{1.97}$.

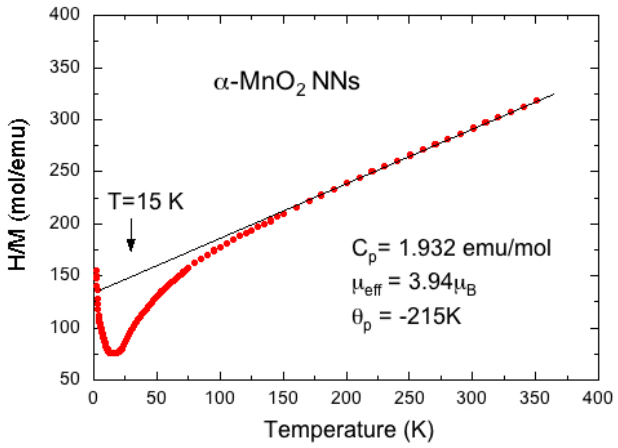

Figure 12. Temperature dependence of the reciprocal magnetic susceptibility, $\chi_m^{-1} = H/M$, of α-MnO_2 nanoneedles. The solid line represents the Curie-Weiss behavior of the paramagnetic region. Reproduced with permission from [43]. Springer, 2016.

Figure 13 presents the charge–discharge profiles of MnO_2-NNs//Li cells vs. specific capacity for cycles up to the 100th [43]. The discharge plateau at ca. 2.35 V corresponding to the reduction of Mn^{IV} ions (lithium insertion) disappears in the first discharge curve and a smooth S-shaped discharge profile is observed in the next cycles. The hollandite α-MnO_2 phase would have a discharge capacity up to

230 mAh·g^{-1} based on a discharge voltage range of 4.0–2.0 V vs. Li^+/Li^0 [81]. The initial discharge capacity is 230 mAh·g^{-1} for our sample, which means about 0.73 Li ions per formula unit inserted into the MnO_2 framework. Note that Li ions prefer to occupy the off-center 8 h site near the (2 × 2) tunnel of the α-MnO_2 lattice, but shift to the 8*h*′ site in α-$Li_{0.75}MnO_2$ lattice due to the Coulomb repulsion between Li ions.

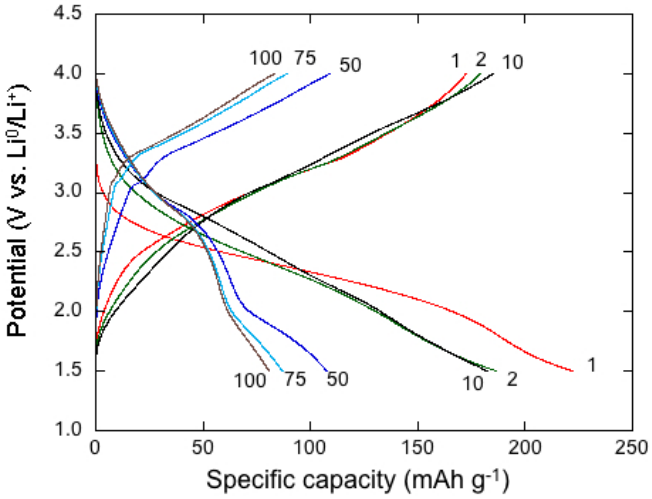

Figure 13. Discharge/charge profiles of Li//α-MnO_2 cell as a function of cycles. Measurements were carried out at C/10 current rate in the voltage range 1.5–4.0 V vs. Li^+/Li^0. Reproduced with permission from [43]. Springer, 2016.

Feng et al. [79] and Li et al. [123] showed that α-MnO_2 urchin-like has better performance than other α-MnO_2 samples due to the morphological sensitivity on the electrochemical performance. The good results of the sea-urchin shape are attributed to the hierarchical structure combining with 1D nanorods, which minimize the Li diffusion path with a 3D nanostructure that exhibits a high specific surface area (~95 m^2·g^{-1}). It is believed that such morphology prevents the formation of a Li-MnO_2 spinel phase. He et al. [124] pointed out similar properties in the case of α-MnO_2 electrodes for supercapacitors, as the MnO_2 nanorods prepared with 0.59 g $KMnO_4$ delivered the highest capacitance of 198 F·g^{-1} with 94% retention after 2000 cycles.

6. Doped-MnO_2 Materials

Doping of MnO_2 frameworks has been successfully realized using metal ions such as Ag^+, Ni^{2+}, Cu^2, Co^{2+}, Fe^{3+}, Cr^{3+}, Mo^{6+}, V^{5+}, W^{6+}, etc. [125–130]. Novel morphologies and enhanced electrochemical properties of the cryptomelane structure(α-K_xMnO_2) are currently obtained by a change of the crystal chemistry by exchange of K^+ ions with protons and/or doping by a single-type metal cation with either low-valence state (3+, 2+, 1+) or high-valence state (5+, 6+). There are two possibilities to insert metal cation as doping element into the a-MnO_2 lattice: (i) substitution of Mn cation in the octahedral framework that implies a six-coordinated cation with a crystal radius similar to that of $^{VI}Mn^{3+}$ low spin (0.72 Å), $^{VI}Mn^{3+}$ high spin (0.785 Å), and $^{VI}Mn^{4+}$ (0.67 Å) and (ii) insertion of the dopant cation into the (2 × 2) tunnel, which allows an eight-coordinated cation with crystal radius similar to K^+ (1.65 Å) [131]. For dopant cations of lower valence, the more negative charge of the lattice favors the incorporation of more K^+ ions into tunnels that enhances the structural stability. Dopant cations of higher valence create an excess of electrical charge that can be compensated by the creation of vacancies, which results in structural distortion and thermal instability.

6.1. Literature Survey

Pure α-MnO_2 is a semiconductor with bandgap 1.44 eV that has an antiferromagnetic ground state due to the symmetric nature of Mn-O-Mn bonds. When the material is prepared through a redox reaction of $KMnO_4$, a large concentration of K^+ ions can be incorporated in the tunnels, which make α-MnO_2 a half-metallic compound; for a potassium content of ≈12 at%, a ferromagnetic-like behavior is observed at low temperatures <5 K [132]. On the other hand, at low potassium content MnO_2 has a poor electronic conductivity ($\approx 10^{-8}$ S·cm^{-1}). Therefore, the control of doping favors the enhancement of ionic and electronic transport. As MDOs crystallize in multiple tunnel structures, MnO_2 shows different electrochemical behaviors with Faradaic reactivity in the sequence δ-MnO_2 > α-MnO_2 > γ-MnO_2 > β-MnO_2, which can tune the ion insertion reactions. It is well-known that the MnO_2 electrode shows gradual capacity fading during long-term cycling due to structural destabilization related to the Jahn-Teller distortion and partial Mn^{3+} dissolution [133]. To overcome this disadvantage of structural destabilization and to enhance the electronic transport in MnO_2 that facilitates the discharge/charge rate of the electrode, doping with various elements, i.e., Ag, Sn, V, Ni, Cu, Al, etc., has been proposed [10,134,135]. The use of selected doping elements allows the properties of α-MnO_2 to be tuned for practical applications. For example, alkali ions such as Li^+ (0.076 nm ionic radius) are easily housed in the (2 × 2) tunnels (0.48 nm size) and can move freely under electrochemical stimulus. Such physical behavior has been applied to batteries and supercapacitors [1].

The role of doping in α-MnO_2 as oxygen reduction reaction (ORR) electrocatalyst has been widely investigated [136]. It was shown that Ni doping stabilizes the Mn^{3+}/Mn^{4+} mediating species involved in ORR activity. Hao et al. [137] synthesized Ni-doped α-MnO_2 nanoneedles via a facile hydrothermal method. The role of nickel was to promote the oxygen reduction reaction in alkaline media, i.e., 0.1 mol·L^{-1} KOH aqueous solution. The electrochemical measurements show that 2.22% Ni-doped MnO_2 has excellent electrocatalytic activity (EA) due to the increment of Mn(III) as electrochemical active sites. High EA was also reported for MnO_2 particles dispersed on high surface area carbon [138]. Davis et al. [139] studied the catalytic activity of Cu-doped α-MnO_2 nanowires. Due to the similarity of the Al^{3+} and Mn^{4+} atomic radius, aluminum can substitute Mn or be located in tunnel of α-MnO_2. Hu et al. [140] showed that Al-doped α-MnO_2 nanoneedles prepared by the hydrothermal method using K-free precursors and $Al_2(SO_4)_3 \cdot 18H_2O$ as dopant reagent were beneficial for pseudocapacitor electrode application with a specific capacitance of 213 F·g^{-1}. Zn-doped MnO_2 nanoparticles (high surface area ~46 m^2·g^{-1}) were prepared by precipitation of $KMnO_4$ and metal acetates with heat treatment of the precipitate at 400 °C for 3 h [141]. Cr^{3+}-ion doping induces a phase transition of MnO_2 from β- to α-polymorph. The size of MnO_2 nanorods increased from 20 to 70 nm with the dopant concentration [142]. Note that insertion of Cr^{3+}-ion is favored in the α-MnO_2 phase because the ionic radius (0.1 nm) is closed to that of K^+ (0.118 nm). A high specific capacitance of 583 F·g^{-1} at current density of 10 A·g^{-1} was obtained with Cu-doped MnO_2 nanorods prepared by precipitation of $KMnO_4$ and copper acetate [143].

6.2. Vanadium-Doped MnO_2

Vanadium-doped MnO_2 nanoparticles were prepared by different routes including the redox reaction [134,144,145]. Alfaruqi et al. [135] used a simple redox reaction between $Mn(CH_3COO)_2 \cdot 4H_2O$ and $KMnO_4$ in aqueous solution added to a solution containing V_2O_5 to obtain α-MnO_2 nanoparticles after annealing at 450 °C for 5 h. This material was used as electrode for zinc-ion batteries. V-doped γ-MnO_2 used as the cathode in primary lithium batteries was prepared by the redox reaction of $KMnO_4$ and $MnCl_2 \cdot 4H_2O$ with V_2O_5 as dopant reagent in a 3:1:0.15 molar ratio. The final products obtained from the precursors annealed at 375 °C for 10 h exhibit an anisotropic expansion that achieved better diffusion coefficient of Li^+ ions in the (1 × 1)/(1 × 2) tunnel frameworks, i.e., ~2 × 10^{-8} vs. ~5 × 10^{-9} cm^2·s^{-1} for pure MnO_2 [146,147].

6.3. Titanium-Doped MnO_2

Li et al. [148] synthesized Ti-doped δ-MnO_2 nanoflakes (with thickness of ≈50 nm) via the anion route for the highly catalytic combustion of benzene. Due to the abundant pore structure and the active oxygen induced by Ti doping, these nanoflakes have the highest catalytic oxidation property over benzene. The interlayer spaces of ~0.7 nm and mesopores of 4–5 nm and 8–9 nm) facilitate gas diffusion and reactions. Ti-containing γ-MnO_2 was prepared in two steps by in situ precipitation technique. First, $MnSO_4$ and $TiOSO_4 \cdot xH_2SO_4$ with various Ti/Mn atomic ratios were dissolved in aqueous solution along with concentrated nitric acid. The second step consisted of the precipitate of $KMnO_4$ with the first solution heated at 90 °C (refluxing). Titanium incorporated into the MnO_2 hollow sphere framework favors electrochemical performance with a high specific capacity (2200 $mAh \cdot g^{-1}$ of carbon) in the Li/air battery and strong oxidative catalytic activity in the toluene oxidation process as well [149]. Nanostructured 5% Ti-doped α-MnO_2 particles were synthesized by hydrothermal methods using two different oxidizing agents, i.e., ammonium persulfate and potassium permanganate for electrocatalytic applications. The doped samples show an efficient oxygen reduction reaction (ORR) activity in alkaline media that leads to a significant shift of the ORR potential (~100 mV) comparable to the well-performing $Pd_{45}Pt_5Sn_{50}$ material [150].

6.4. Al, Cu, Mg-Doped MnO_2

The advantage of the Mn to Al substitution in γ-$Mn_{1-y}Al_yO_{2-\delta}$ interconnected nanowires was an increase of the surface area from 17 to 184 $m^2\ g^{-1}$ for y(Al) = 0.11, which resulted in an increase of the Faradic behavior [151]. Pure MnO_2 and its M-doped MnO_2 (M = Al, Cu, Mg) were prepared by redox reaction of $KMnO_4$ and fumaric acid ($C_4H_4O_4$) [152]. Both pure and doped samples show the same characteristic peaks of cryptomelane-MnO_2 ($K_2Mn_8O_{16}$). No extra peaks related to Al, Cu, and Mg compounds are observed. No diffraction lines associated with doping elements were observed, which can receive three interpretations: (i) transition metal oxides are in low content or have crystalline domains beyond the detection limit of XRD; (ii) transition metals are incorporated in the cryptomelane structure, with the formation of a solid solution; and/or (iii) transition metals are incorporated into the channels of the K_xMnO_2 structure, replacing K^+ ions [19], All possible reflections of cryptomelane compounds are present in the prepared samples. The MnO_2 lattice of all samples is related to the presence of K^+ ions inside the (2 × 2) tunnels of the prepared samples as observed. Chemical analysis shows that the amounts of potassium (in %) for P-MnO_2, Al-MnO_2, Cu-MnO_2, and Mg-MnO_2 samples are 0.7, 7.9, 5.6, and 8.9, respectively. Chemical analysis shows also that the percentages of Al, Cu, and Mg in the doped samples are 0.4, 0.6, and 0.3, respectively.

The electronic transport measurements were performed below room temperature (RT) by the Van der Pauw four-point method. All four MDOs show a semi-conducting behavior at RT with a decrease of resistivity by three to four orders of magnitude depending on the dopant. The Al-MnO_2 sample has the lowest resistivity between the four oxides. Above RT, the electrical resistivity ϱ was activated, as can be deduced from the linear dependence of the ln (ρ) as a function of $1/T$ reported in Figure 14. The activated band gaps E_g of the four oxides determined from the slope of these linear curves show that the gap of parent MnO_2 is close to the value of 0.69 eV obtained for γ-MnO_2 and to the value of 0.58 eV obtained for cryptomelane MnO_2 [153]. Doping reduced E_g to a value close to 0.34 eV, close to the value 0.26–0.3 eV reported for β-MnO_2 [154]. The introduction of dopant ions like Al, Cu, and Mg seems to stabilize the MnO_2 structure and hence reduce the capacity fading observed for pure MnO_2. The presence of a low concentration of stabilizing atoms within the (2 × 2) tunnel of a cryptomelane- or hollandite-type framework is required to facilitate the diffusion of Li ions during charge–discharge cycling as observed for doped α-MnO_2 samples [152].

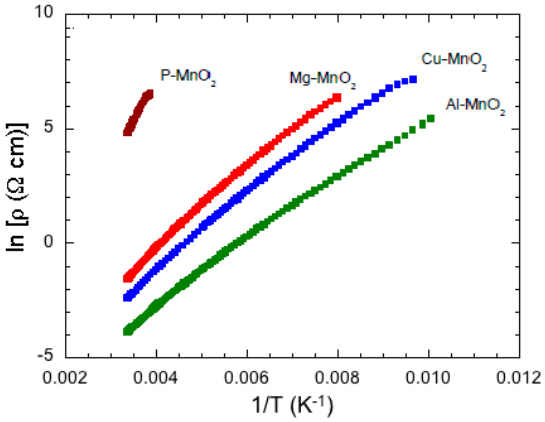

Figure 14. Plots of ln(ϱ) vs. 1/T of pure and *M*-doped K_xMnO_2 (*M* = Al, Cu, Mg) samples. Reproduced with permission from [152]. Elsevier, 2011.

6.5. Tin-Doped α-MnO_2

To prevent the transformation from α-MnO_2 to α-Mn_2O_3 that takes place in the temperature range of 500–600 °C, doping with Sn and Co was proposed by Hashem et al. [155]. Samples were synthesized in an acidic medium using the reduction of $KMnO_4$ by fumaric acid (10:3 molar ratio) with addition of $SnCl_2$ as Sn dopant source. Final products were obtained by heat treatment at 450 °C for 5 h. Figure 15 shows the thermogravimetric analysis (TGA) of the pristine and Sn-doped MnO_2 samples heated in the range 30–1000 °C in air. The TGA curve for the undoped sample shows a slight weight loss (ca. 3%) due to the removal of surface and structural water and an abrupt weight loss at ca. 540 °C due to the exothermic reaction of the phase transition from α-MnO_2 to Mn_2O_3 and release of oxygen. TGA curves of α-MnO_2:Sn illustrate the structural stability of the doped samples up to 850 °C. This effect of the introduction of a small concentration ≈5% of Sn into the crystal lattice, is attributed to the fact that the doping maintains the tunnel structure of α-MnO_2. The magnetic susceptibility measurements confirm this stabilization effect. At high temperature $T > 150$ K, MnO_2 exhibits Curie-Weiss paramagnetic behavior, while a ferromagnetic contribution is observed at low temperature ($T < 30$ K), due to the 180° Mn^{3+}-O-Mn^{4+} bridge. The increase of dopant concentration decreases the Mn^{3+} content and reduces the ferromagnetic content.

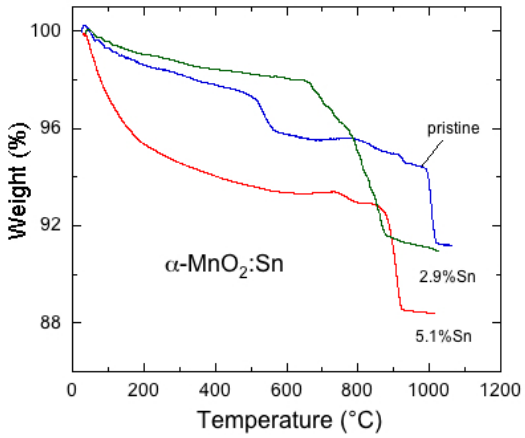

Figure 15. Thermogravimetric analysis of pristine and Sn-doped MnO_2 samples heat treated in the range 30–1000 °C in air at heating rate 10 °C/min. Reproduced with permission from [155]. Springer, 2008.

Figure 16 shows the electrical conductance σ_{ac} vs. frequency for α-MnO_2 samples with different Sn or Co dopant concentrations. Results show the typical features of a semiconducting material with a frequency dependence that obeys the power law:

$$\sigma_{ac} = \sigma_{dc} + A\omega^n, \quad (14)$$

where the low-frequency value corresponds to the direct-current conductivity σ_{dc}, n is the power exponent, and A is a constant. An increase in the electrical conductivity is clearly observed in the presence of dopant in comparison with the pristine α-MnO_2 material. It is believed that free electrons of Co(II) and Sn(II) contribute to the increase of the conductivity of the doped samples.

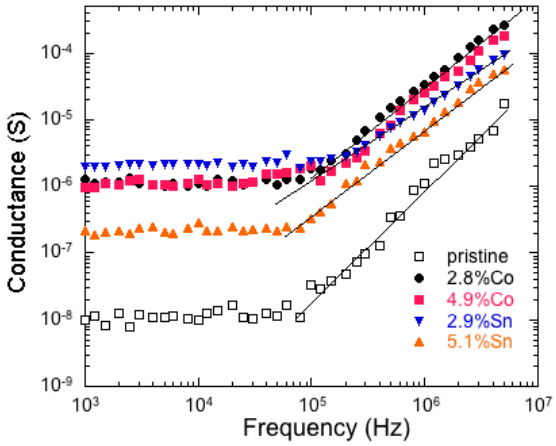

Figure 16. Electrical conductance as a function of frequency for α-MnO_2 samples with different Sn or Co dopant concentrations. Reproduced with permission from [155]. Springer, 2008.

Hashem et al. [10] investigated the electrochemical performance of Sn-doped α-MnO_2 nanorods-like particles. The specific discharge capacities vs. the cycle number for P-MnO_2 and Sn–MnO_2 are shown in Figure 17. Capacities are ~65 and ~80 mAh g^{-1} for the P-MnO_2 and Sn-MnO_2 electrodes at the 40th cycle, respectively. These results show that capacity fading of the pristine electrode is much higher than that of Sn-doped MnO_2. The electrochemical performance and the structural stability are attributed to the decrease of Mn^{3+} Jahn-Teller ions upon insertion of Sn ions into the (2 × 2) tunnels. The second reason for the electrochemical degradation of pristine MnO_2 is due to the reduction of Mn^{2+} ions, which dissolve in the electrolyte.

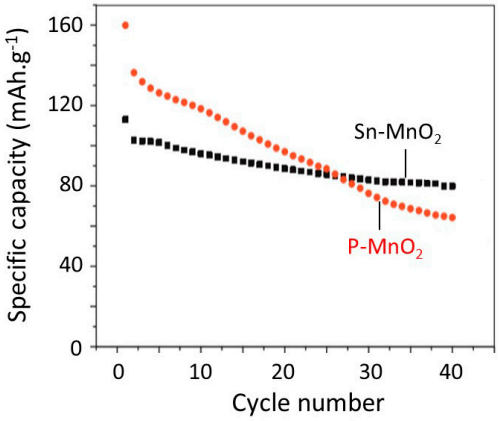

Figure 17. Discharge capacity vs. cycle number of P-MnO_2 and Sn-doped MnO_2 at C/15 rate in the voltage range 1.5–4.0 V vs. Li^+/Li^0. Reproduced with permission from [10]. Elsevier, 2011.

6.6. Ag-Doped MnO_2

Pristine K_xMnO_2, Ag-doped and Ag-coated K_xMnO_2 materials ($x \approx 0.065$) were obtained by a simple wet-chemical process. Then the particle size was reduced to ~20 nm by re-stirring the as-prepared oxides in de-ionized water for 24 h at RT [156]. Elemental analyses show a concentration of silver 1.4% and 3.9% in doped and coated K_xMnO_2, respectively. From magnetic measurements the Ag-coated K_xMnO_2 sample shows an increasing Mn^{+4}/Mn^{+3} ratio and hence a reducing amount of Jahn-Teller Mn^{+3} ions. The net result is a better electrochemical performance of Ag-coated K_xMnO_2 (Figure 18). For the Li//MDO cells cycled up to 40th cycle, the discharge specific capacities are 115, 110, and 90 $mAh \cdot g^{-1}$ for Ag-coated K_xMnO_2, pure K_xMnO_2, and Ag-doped K_xMnO_2 samples, respectively. The Ag-coated K_xMnO_2 sample showed the best results for capacity retention due to nanosized particles obtained by stirring in deionized water and to enhanced conductivity after Ag coating.

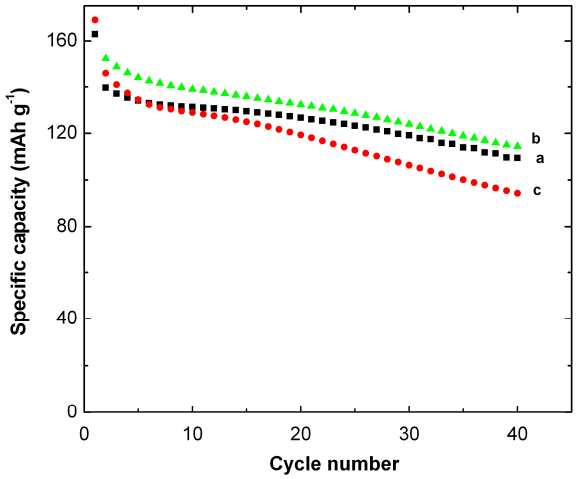

Figure 18. Specific discharge capacity vs. cycle number of Li//MDO cells with (**a**) pure; (**b**) Ag-coated; and (**c**) Ag-doped K_xMnO_2 samples. Discharge processes were conducted at C/5 rate in the voltage range 1.5–4.0 V vs. Li^+/Li^0. Reproduced with permission from [156]. Elsevier, 2011.

6.7. Co- and Ni-Doped MnO_2

Cobalt-doped α-K_xMnO_2 was synthesized following the same process used for tin-doping, except that the Sn precursor was now replaced by $Co(NO_3)_2 \cdot 6H_2O$ as Co dopant source in a molar ratio 3:1:0.07, respectively [157]. Table sugar was the source of carbon for coating. Chemical analysis gives the chemical stoichiometry $K_{0.009}MnO_2$ for the pure sample and $K_{0.095}Co_{0.013}MnO_2$ for the doped sample. Both electrochemical inactive Co^{3+} and K^+ ions are trapped inside the large tunnel (4.6 Å width). The additional effect of Co doping and carbon coating results in a good rechargeability and a decrease of capacity fading at the expense of the initial capacity (Figure 19). The carbon layer acts as a protective film surrounding the particles and favors the charge-transfer rate of Li^+ insertion/extraction reactions. Magnetic properties indicate that the mixed valence state Mn^{4+}/Mn^{3+} with low concentration of Mn^{3+} decreased after the coating and doping process.

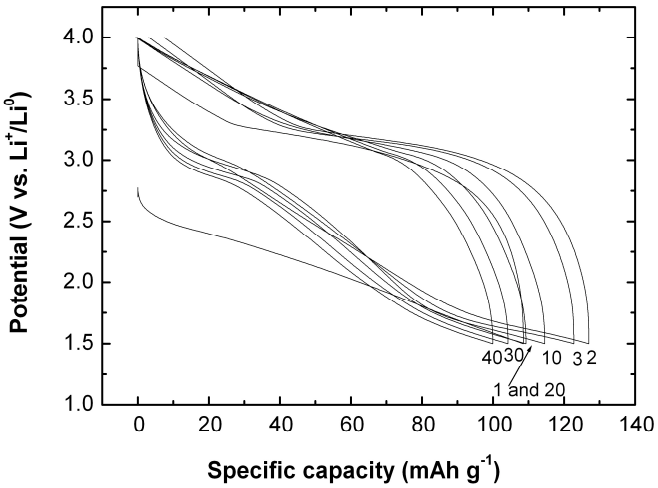

Figure 19. Charge/discharge curves of Co-doped $K_{0.095}MnO_2$. Cycles operated in voltage range 1.5–4.0 V vs. Li^+/Li^0 at C/15 rate. Reproduced with permission from [157]. Springer, 2012.

Nanospheres of 5 wt % Co-doped R-MnO_2 (diameters in the range 350–500 nm) composed of nanoflakes 3 nm thick were grown with a yolk-shell structure using a redox reaction of $K_2S_2O_8$ and $MnSO_4 \cdot H_2O$ with added $CoSO_4 \cdot H_2O$ [158]. These nanospheres had specific surface area 135 $m^2 \cdot g^{-1}$ with pore size of 9 nm. Korosec et al. [159] reported the structural properties and thermal stability of cobalt- and chromium-doped α-MnO_2 nanorods synthesized by decomposition of $KMnO_4$ in an acidic environment. EXAFS studies showed that both dopant ions (Co^{2+}, Cr^{3+}) substitute Mn^{4+} in the center of an octahedron increasing the negative charge of the lattice compensated by an increase of K^+ ion concentration in the tunnels. In another work [160], Co/Ni-doped $K_{0.14}MnO_2$ tetragonal phase (cryptomelane structure) was synthesized via a common redox reaction with metal sulfates as dopant agents. The mole fractions of Ni^{2+} and Co^{2+} in the final product were 2% and 7%, respectively. The samples were composed of nanowires of diameter 15–20 nm, length of 100–300 nm. The Co/Ni doping did not modify the 1D nanostructure of α-MnO_2, because of the growth mechanism of the dissolution–recrystallization process. Co-doped birnessite (Co-bir) δ-MnO_2 is a catalyst synthesized by a modified sol-gel method for the oxidation of benzylic alcohols to benzaldehydes achieved in heated toluene under oxygen atmosphere [161]. The enhanced electrical conductivity of δ-MnO_2 is attributed to location of Co^{2+} ions in the octahedral lattice.

A different result was reported by Biswal et al. [162] who found different morphologies depending on whether the dopant is Co or Ni. The synthesis process was also different from the previous one: a galvanostatic method, starting from manganese sulfide in sulfuric acid medium. Note this preparation misses the presence of K^+ ions that was found to be so important in this review to stabilize the material and optimize the electrochemical properties of the α- and β-MnO_2 phases. It is also important that these EMD samples were found in a different phase, namely the γ-MnO_2 phase. One of these samples was prepared with Ni- and the other one with Co- in situ doping. With Co-doping, the EMD was synthesized with the form of cauliflowers, while the EMD with Ni-doping was sea-urchin shaped. In both cases, the doping increased the energy density, but not at the same level: 395 $mAh \cdot g^{-1}$ for Ni-doping, against 670 $mAh \cdot g^{-1}$ for Co-doping; on another hand, the cycling life was better with Ni-doping. Therefore, in any phase, the Co or Ni doping increased significantly the conductivity and the electrochemical properties. However, in [162], the increase of conductivity in Co-doped EMD was attributed to the presence of Co_3O_4. It would be of interest to conduct Raman experiments to verify this hypothesis.

6.8. Bismuth-Doping and Additives

The incorporation of Bi^{3+} cations has been known to be beneficial to the electrochemical properties of MDO for many years, irrespective of the crystal phase [163–166]. This improvement includes an increase of the conductivity like the introduction of the other dopant ions, but in addition, a specific property of the bismuth is that it reduces the formation of the spinel structure [167], which is responsible for irreversibility of the MnO_2 cells, as the Mn_3O_4 spinel is not electroactive. The reason why Bi has such an important effect has been described by Yu [168] who noticed that the ionic radius of Bi^{3+} being much larger than the ionic radii of Mn^{2+} and Mn^{3+}, they cannot insert into the spinel lattice, which prevents the formation of the spinel along the chain of reactions during the synthesis of MnO_2. This important role of bismuth was also observed more recently by Im and Manthiram [169] who incorporated Bi^{3+} cations into γ-MnO_2 with the Bi_2O_3 additive in an alkaline electrolyte. Comparing the effect of Ti- and Bi-incorporation on the electrochemical properties of γ-MnO_2, Sundaram et al. [170] found that Ti is even more efficient than Bi in preventing the formation of Mn_3O_4. In addition, they found that even better electrochemical properties were obtained by multiple additives. In particular, the synergetic effect of adding 3 wt % Bi_2O_3 plus 2 wt % TiS_2 led to a superior capacity of 240 $mAh{\cdot}g^{-1}$, much larger than the results found with Bi_2O_3 or TiS_2 only.

Other additives that have improved the electrochemical properties of γ-MnO_2 are TiB_2, CeO_2, MgO, and B_4C [171–175]. Several reports have shown the irreversible dissolution of Mn^{3+} ions in alkaline KOH solutions. This reaction leads to the growth of electrochemically inactive phases, for example δ-MnO_2 and Mn_3O_4. Not surprisingly, the additives that can suppress the dissolution of the Mn^{3+} ions are also those which have been shown to prevent the formation of Mn_3O_4 such as TiB_2, Bi_2O_3, and also Ba-containing compounds [176].

7. MnO_2 Polymer Composites

MnO_2 is a material that can be combined with various polymers to make nanoarchitecture hybrids as highly performing electrode materials for pseudocapacitive devices. A blend formed by electrochemical polymerization of pyrrole monomer (Py) on prepared manganese dioxide powders was studied as the electrode for a supercapacitor [110,177]. The capacitance of the MnO_2 electrode is predominantly pseudocapacitive, which is attributed to reversible redox transitions involving exchange of protons and/or cations with the electrolyte. In practice, the MnO_2 specific capacitance is ~200–300 $F{\cdot}g^{-1}$ due to its intrinsically poor electronic conductivity, size of particles, and porosity of the oxide [53]. γ-MnO_2, i.e., $(1 \times 1)/(1 \times 2)$ tunnel structure, was prepared by a precipitation method of $MnCl_2{\cdot}4H_2O$ and $KMnO_4$ in distilled water and dried at 110 °C for 10 h.

7.1. Polypyrrole-Coated MnO_2

The electrodeposition of polypyrrole (PPy) was carried out with a chronoamperometry test at a monomer oxidation potential 900 mV vs. SCE. The net effect of the PPy deposit is an increase of the BET surface area for PPy/γ-MnO_2 of 125 $m^2{\cdot}g^{-1}$ vs. 64 $m^2{\cdot}g^{-1}$ for γ-MnO_2. Figure 20 shows the SEM images of pristine and γ-MnO_2 particles covered with electrodeposited PPy. We observe that the electrochemical polymerization process does not change the morphology of the MnO_2 grains and that MnO_2 particles synthesized by the precipitation route have a regular shape with an average grain size 250 nm [177].

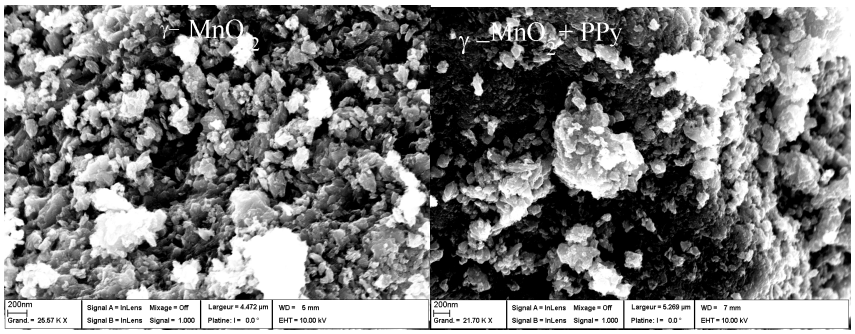

Figure 20. SEM images of γ-MnO_2 particles (**left**) and grains covered with electrodeposited PPy for 40 min (**right**). Reproduced with permission from [177]. The Electrochemical Society, 2013.

The MnO_2 and PPy/MnO_2 pseudocapacitance is due to the Mn^{4+}/Mn^{3+} reversible redox reaction accompanied by a reversible insertion/desinsertion of alkali cation (Na^+) or protons H_3O^+ present in the electrolyte:

$$MnO_2 + Na^+ + e^- \rightarrow MnOONa. \quad (15)$$

The specific capacitance was determined from galvanostatic charge-discharge cycling tests at a constant current density 2 $mA{\cdot}cm^{-2}$ [110]. The asymmetric supercapacitor with PPy/γ-MnO_2) composite cathode and carbon anode has high specific capacitance of ~142 $F{\cdot}g^{-1}$ vs. ~74 $F{\cdot}g^{-1}$ for γ-MnO_2. Note that the specific capacitance of PPy/MnO_2 materials is proportional to the thickness of the PPy deposit. The performance of the composite material was measured in a constant charging–discharging experiment at a discharge current density 2 $mA{\cdot}cm^{-2}$ over 500 cycles (Figure 21). The stabilization of the specific capacitance indicates that the electrode had regular capacitive behavior and good cycling stability.

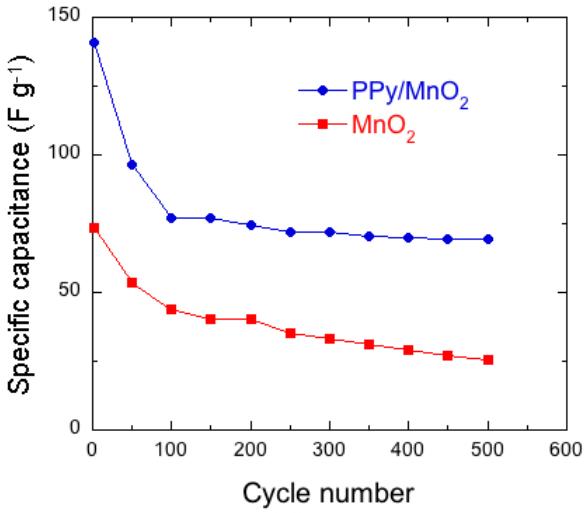

Figure 21. The variation of specific capacitance of PPy/MnO_2 electrode vs. cycle number. Charge and discharge experiments were carried out at 2 $mA{\cdot}cm^{-2}$. Reproduced with permission from [110]. Elsevier, 2013.

Note, however, that the DMO-polymer association does not give the best supercapacitor. For comparison, the aqueous asymmetric capacitor with EMD obtained from a leach liquor derived from manganese ore/residue delivered a capacity of 50 $F{\cdot}g^{-1}$. The outstanding performance with respect to the results we reported above, however, is the cycling life, since 100% capacity was retained after 2000 cycles [98].

7.2. Polybithiophene-Coated MnO_2

A new composite formed by polymeric polybithiophene (PBTh) and crystallized MnO_2 was applied as a p-n heterojunction with good photoconducting performance in solar cells. The PBTh/MnO_2 sample was deposited on an indium tin oxide (ITO) substrate. Incorporation of MnO_2 particles into the polymer films greatly increases the generated photocurrent from 5.9 $\mu A \cdot cm^{-2}$ for ITO/PBTh up to 20.6 $\mu A \cdot cm^{-2}$ for the ITO/PBTh-MnO_2 films with 100 mg MnO_2 incorporated [178].

Similarly, a polymer/inorganic composite was used as cathode material in Zn//γ-MnO_2 electrochemical cells. The composite was prepared by electrodeposition of PBTh on MnO_2 particles in 0.01 $mol \cdot L^{-1}$ PBTh/0.1 $mol \cdot L^{-1}$ $LiClO_4$ in acetonitrile (CH_3CN) solution [179]. The performance of MnO_2 electrodes was tested by EIS experiments for both discharged Zn//MnO_2 and Zn//PBTh + MnO_2 cells (see Figure 22). The Nyquist plots display EIS profiles containing a semicircle (high-frequency range) and a quasi-linear line (low-frequency range). The semicircle is due to the charge transfer resistance (R_{ct}) of the cathode material in relation to the contact between particles. The quasi-linear part at low frequency is the Warburg contribution of proton diffusion through the bulk of the material. The fit illustrated in Figure 22 gives a charge transfer resistance R_{tc} = 4.49 $\Omega \cdot cm^{-2}$ for Zn//MnO_2 cell and reduces to R_{tc} = 3.42 $\Omega \cdot cm^{-2}$ for the Zn//PBTh + MnO_2 cell.

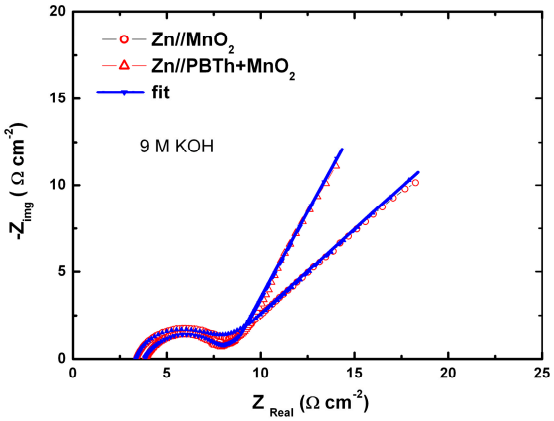

Figure 22. Nyquist plots of the Zn//MnO_2 and Zn//PBTh + MnO_2 cells. Reproduced with permission from [179]. Elsevier, 2011.

Figure 23 presents the electrochemical profile of Zn//MnO_2 and Zn//MnO_2 + PBTh cells discharged at current density of j = 2 $mA \cdot cm^{-2}$ [17]. A continuous decrease of the cell voltage is observed in the 1.45–0.9 V potential range. No plateau can be observed. The capacity of the Zn//MnO_2 + PBTh cell is 25% higher than that of the Zn//MnO_2 cell. The overall cathodic reaction that reduces MnO_2 to MnOOH, involves a solid-state diffusion process for protons moving from the surface to the interior of the MnO_2 grains, as follows:

$$H_2O\ (1) \rightleftarrows H^+\ (\text{surface}) + OH^-\ (aq), \tag{16}$$

$$H^+\ (\text{surface}) \rightarrow H^+\ (\text{bulk}), \tag{17}$$

$$x MnO_2 + H^+\ (\text{bulk}) + e^- \rightarrow (MnO_2)_{x-1}\ (MnOOH)\ (s). \tag{18}$$

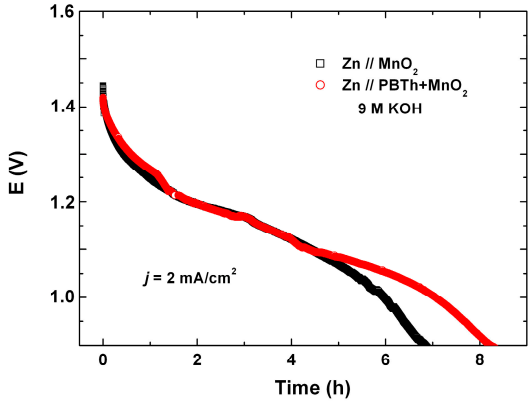

Figure 23. Discharge profiles of the Zn//MnO_2 and Zn//PBTh/MnO_2 cells discharged at current density 2 mA·cm^{-2}. Reproduced with permission from [179]. Elsevier, 2011.

The conducting polymer coat on MnO_2 particles has an important role. First, it favors the diffusion of protons; second, the conducting polymer can be reduced during discharge or can occupy the pores, which results in more active material and a larger effective surface area. Composite materials of conducting polymer and β-MnO_2 were prepared by electrodeposition in CH_3CN/0.1 mol·L^{-1} $LiClO_4$ cell of conducting polymer on a β-MnO_2 surface with different monomers: bithiophene (BTh) or pyrrole (Py) in CH_3CN/$LiClO_4$ (0.1 mol·L^{-1}) [180]. A successful electro-polymerization requires the formation of a layer able to inhibit the dissolution of the oxidant metal. At the same time, however, access of the monomer must be kept allow for its further oxidation. It is known that MDO could catalyze oxygen reduction reaction (ORR), which occurs via a two-electron reduction mechanism in alkaline solution with the formation of hydrogen peroxide ion (HO_2^-). β-MnO_2 was chosen because, with its (1 × 1) tunnel structure (rutile-type), it has the best structural properties among the MDOs.

Figure 24 shows the cyclic voltammograms recorded for O_2 reduction in O_2 saturated 2 mol·L^{-1} KOH solution (solid line) vs. argon saturated solution (dashed line). The O_2 reduction peak occurs at −506 and −365 mV for PBTh/β-MnO_2 and PPy/β-MnO_2 electrodes, respectively. The enhanced electrocatalytic effect of PPy/β-MnO_2 can be witnessed by a significant positive shift of the O_2 reduction potential from −412 to −365 mV and a decrease in the O_2 reduction peak current from 289 to 83 μA·cm^{-2}. In addition, PBTh/β-MnO_2 is gifted with very good electrocatalytic activity for ORR owing to more negative onset potential than β-MnO_2.

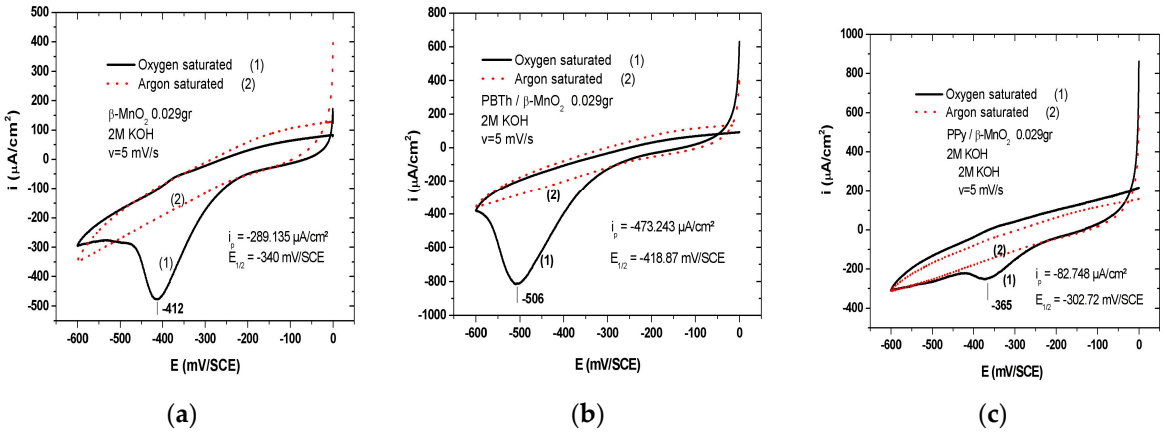

Figure 24. Cyclic voltammograms of β-MnO_2 (**a**), PBTh-MnO_2 (**b**) and PPy-MnO_2 (**c**) in 2 mol·L^{-1} KOH electrolyte in the potential range 0–600 mV/SCE at scan rate 5 mV·s^{-1}. The results are reported in oxygen saturated: solid line, (1) and in argon saturated solution: dotted line, (2). Reproduced with permission from [180]. Springer, 2011.

8. Nanocomposites

An ideal nanocomposite electrode, for supercapacitors, that possesses long cycle stability should contain a high-power density material (carbon-based) associated with a high-energy density compound (oxide). MnO_2 has high theoretical specific capacitance (1380 $F{\cdot}g^{-1}$) but its main disadvantage is poor conductivity (10^{-5}–10^{-6} $S{\cdot}cm^{-1}$) that can be enhanced by the fabrication of various MnO_2/conductive matrix hybrid materials such as SnO_2/MnO_2 [181], multiwalled carbon nanotube (MWCNT)/MnO_2 [182] and C/MnO_2 nanomaterials [183].

8.1. MnO_2-Carbon Nanocomposite

For example, Chen et al., deposited MnO_2 nanoparticles on graphene oxide (GO) sheets that enhanced the electrochemical properties due to the chemical interaction between MnO_2 and GO [184]. Lv et al. [185] demonstrated the superior cycling performance (97% after 5000 cycles) of the nanocomposite formed by N-doped carbon tubes and Au-doped MnO_2 nanoparticles. Fan et al. [186] proposed a new composite of carbon nanotubes (CNTs)/graphene, composed of CNT pillars sandwiched between the graphene sheets that showed a specific capacitance as high as 385 $F{\cdot}g^{-1}$. Graphenes decorated with flower-like MnO_2 nanostructures were fabricated by electrodeposition for electrodes of supercapacitors. The MnO_2 nano-flowers consisted of tiny rods with a thickness of less than 10 nm. The specific capacitance after the MnO_2 deposition was 328 $F{\cdot}g^{-1}$ at a charging current of 1 mA with an energy density of 11.4 $Wh{\cdot}kg^{-1}$ [187]. Song et al. [188] fabricated a nanocomposite for a supercapacitor composed of needle-like MnO_2 nanowire arrays on graphene synthesized by in-situ growth of MnO_2 nanowires on the surface of graphene nanosheets (GNS). The preparation is a simple redox reaction between $KMnO_4$ and GNS, which can produce the composite at large scale at low cost. The nanocomposite exhibited high-capacitance performance of 276 $F{\cdot}g^{-1}$ at 0.5 $A{\cdot}g^{-1}$. MnO_2 nanoparticle enriched poly(3,4-ethylenedioxythiophene) (PEDOT) nanowires were fabricated by simply soaking the PEDOT nanowires in $KMnO_4$ solution [189]. Due to their extremely high surface area the MnO_2 nanoparticles showed very high specific capacitance (410 $F{\cdot}g^{-1}$) as supercapacitor electrode materials, as well as high storage specific capacity (300 $mAh{\cdot}g^{-1}$) as cathode materials for the Li ion battery [190].

Long et al. [190] prepared ultrathin polymer coatings (10-nm thick) onto nanostructured birnessite-type MnO_2. The composite formed by electrodeposition of poly(*o*-phenylenediamine), which preserved the mesoporosity of MnO_2, showed good stability as electrode material in acid electrolytes. Yan et al. [191] investigated the compatibility of MnO_2 nanowires with SnO_2 to make a high performing electrode for supercapacitors. A specific capacitance of 800 $F{\cdot}g^{-1}$ was achieved at a current density of 1 $A{\cdot}g^{-1}$ in 1 $mol{\cdot}L^{-1}$ Na_2SO_4 aqueous solution. MnO_2 nanowires were electrodeposited onto carbon nanotube (CNT) paper by a cyclic voltammetry technique [28]. This MnO_2 nanowire/CNT composite used as a flexible electrode for electrochemical supercapacitors displayed specific capacitances as high as ~167 $F{\cdot}g^{-1}$ at a current density of 77 $mA{\cdot}g^{-1}$ with faradic efficiency of 88% after 3000 cycles.

8.2. Organo-MnO_2

Composites termed as "organo-MnO_2" can host organic guest species that can capture and detect iodine in organisms and the environment (essential element in thyroid hormones). Such a composite layered δ-MnO_2 structure was synthesized by electrodeposition of $MnSO_4{\cdot}5H_2O$ and $CoSO_4{\cdot}7H_2O$ in aqueous solution in the presence of a cationic surfactant, cetyltrimethylammonium (CTA) [192]. Electrodeposition of the films was performed at constant potential of +1 V with a fixed charge of 200 $mC{\cdot}cm^{-2}$. The oxidation of inserted Co^{2+} ions took part of the deposition process of MnO_2 at 70 °C. CTA molecules occupying the MnO_2 interlayer have the role of a sensing element that could extract I^- ions for solutions, while the Co-framework ions dopant achieved fast electron kinetics for the oxidation of I^- ions [192].

8.3. SnO_2-MnO_2 Composites

To improve significantly the electrochemical performance, MnO_2 particles can be coated with a conductive material, namely a thin SnO_2 layer (~20 nm). In addition, the particles are mixed with a few percent of conductive carbon that percolates through the structure and thus makes electrical contact between the particle and the current collector. Therefore, once an electron of any MnO_2 particle has reached any point of the surface of the particle, it can be driven by the electrical field up to the current collector through the conductive carbon in contact with the conductive SnO_2 layer. On the contrary, in the absence of carbon, even if the particles were coated with a SnO_2 layer, the electron would have to pass from one particle to the other one by the contact point between the particles so that the material would be insulating. This is illustrated in Figure 25.

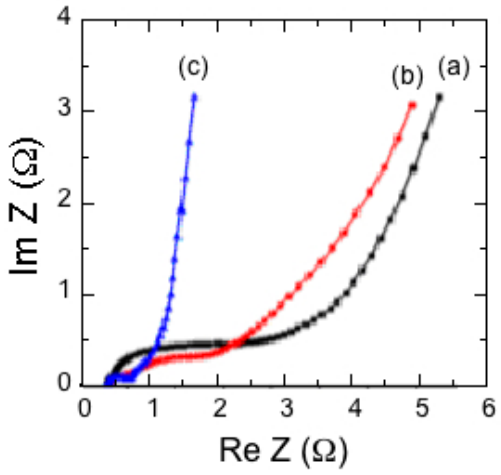

Figure 25. Nyquist plots of (**a**) pristine; (**b**) SnO_2-coated; and (**c**) Sb-doped SnO_2-coated MnO_2 particles. Reproduced with permission from [25]. Elsevier, 2014.

On the other hand, if the particles were not coated, the electrical charge would not be homogenously distributed on the surface along the direction of the electrical field, so that the effective surface area ε_c would be much smaller that the surface area of the particle. This is also illustrated in Figure 25, where the Nyquist plots recorded by electrochemical impedance spectroscopy (EIS) show a large decrease of charge transfer resistance R_{ct} occurring after coating. A decrease of R_{ct} allows high rates for the charge/discharge (deinsertion/insertion) process [25].

To reduce the Mn dissolution in organic electrolyte by surface protection, SnO_2-MnO_2 composite powders were investigated by Hashem et al. [193], who also reported their electrochemical properties. Yan et al. [191] investigated the compatibility of MnO_2 nanowires with SnO_2 to make a high performing electrode for supercapacitors. A specific capacitance of 800 F g^{-1} was achieved at current density of 1 A·g^{-1} in 1 mol·L^{-1} Na_2SO_4 aqueous solution. Nanosized SnO_2-MnO_2 composites were prepared by the wet-chemical method [142] based on a redox reaction between $KMnO_4$ and Mn(II) acetate. The SnO_2-coated samples were obtained from $SnCl_2$ as coating agent. The TEM micrographs of α-MnO_2 and SnO_2/α-MnO_2 are shown in Figure 26. These images indicate that the samples had almost spherical morphology [193]. Both α-MnO_2 and SnO_2/MnO_2 samples were nano-sized particles with a narrow size distribution centered at 200 nm.

The elemental analysis (ICP) shows a concentration of potassium ions of 5.5 mol% in SnO_2/α-MnO_2 samples. In α-MnO_2, the presence of Mn^{3+} originates from insertion of K^+ ions in the tunnel and from oxygen vacancies. Therefore, a small oxygen deficiency results in large crystallite strains and lattice distortions, because Mn^{3+} is a Jahn-Teller ion. This was also evidenced by magnetic susceptibility measurements. For the coated sample, this residual concentration of Mn^{3+} ($3d^4$ configuration) in the low-spin state (spin $S = 0$) is responsible for a decrease of the magnetic moment.

The lower value for μ_{eff} = 3.87 μ_B is due to the presence of K^+ ions in the (2 × 2) tunnels that have the chemical formula $K_yMn^{4+}{}_{8-y}Mn^{3+}{}_xO_{16-z}$, where z is the concentration of oxygen vacancies and $x = y + 2z$ the amount of Mn^{3+}. The experimental results give x = 8.2% in pristine (P)-MnO_2, decreasing to 6.2% in SnO_2/MnO_2. Since y = 5.5 at%, the concentration of oxygen vacancies is z = 1.3 at% in P-MnO_2 and decreases to z = 0.3 at% in the SnO_2/MnO_2. Therefore, the SnO_2 coating has protected MnO_2 against the loss of oxygen.

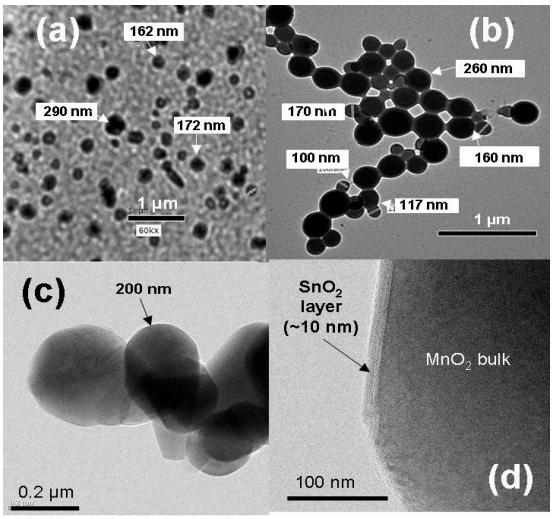

Figure 26. TEM micrographs of P-MnO_2 (**a**) and SnO_2-coated MnO_2 (**b**) powders synthesized by the oxidation method of Mn acetate by $KMnO_4$ at 60 °C. The precursor was fired at 450 °C for 12 h in air. HRTEM images (**c**,**d**) taken at higher magnification shows the spherical particle of the pristine materials and SnO_2-coated with a thin layer 10 nm thick, respectively. Reproduced with permission from [193]. Elsevier, 2012.

Figure 27 shows the discharge curves for Li cells with α-MnO_2 and SnO_2-coated MnO_2 electrode material using 1.0 mol·L^{-1} $LiPF_6$ in ethylenecarbonate- diethylcarbonate (EC-DEC) as electrolyte at the 1st and 45th cycle. It is obvious that the SnO_2 deposit acts as a protective layer around MnO_2 particles which prevents dissolution of Mn-ions into the organic electrolyte.

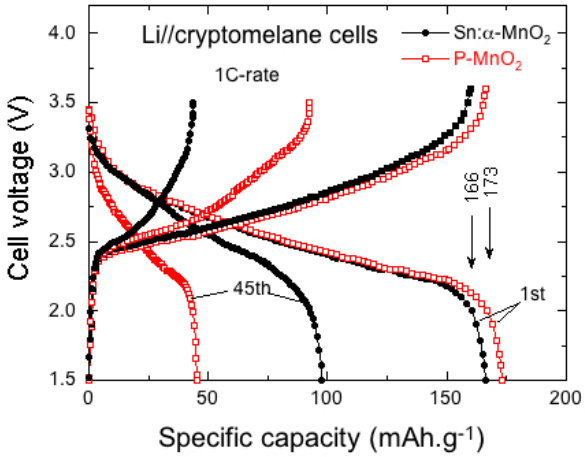

Figure 27. Discharge-charge curves for Li cells with P-MnO_2 and SnO_2/MnO_2 electrode materials. The electrolyte was 1 mol·L^{-1} $LiPF_6$ in a mixture of ethylene carbonate (EC) and diethyl carbonate (DEC) (1:1, v/v). Data were collected at 1C rate in potential range 1.5–3.5 V vs. Li^+/Li^0. Reproduced with permission from [193]. Elsevier, 2012.

9. Concluding Remarks

The new technologies require urgently flexible and wearable energy storage devices. In this context, a breakthrough has been achieved by Zeng et al. [194], who reported a flexible quasi-solid-state Zn-MnO_2 battery with sandwiched structure consisting of a MnO_2@PEDOT (poly(3,4-ethylenedioxythiophene)) cathode, a Zn nanosheet anode ≈50 nm in thickness homogeneously grown on the carbon fibers without any binder, a separator, and a modified poly(vinyl alcohol) (PVA)/1 mol·L^{-1} $ZnCl_2$/0.4 mol·L^{-1} $MnSO_4$ gel electrolyte. The PEDOT shell ≈9 nm in thickness was used as a protection layer to increase the cycling life. This as-fabricated flexible quasi-solid-state battery had an energy density of 505 Wh·kg^{-1} (34 mWh·cm^{-3}) and peak power density 8.6 kW·kg^{-1}. It maintained 78% of its initial capacity (282.4 mAh per gram of MnO_2, 91.6 per gram of the total cathode) and nearly 100% coulombic efficiency after 300 cycles at current density 1.86 A·g^{-1}. An amount of 61.5% of the initial capacity was retained after 1000 cycles. This performance outperforms the most recently reported quasi-solid-state batteries. The great potential of Zn-MnO_2 as a flexible energy storage device combining low cost, safety, high energy density, and environmental friendliness is confirmed by the results obtained by Qiu et al. [195] using MnO_2 nanorod arrays and Zn nanoparticles uniformly deposited on N-doped porous carbon cloth as the free-standing cathode and anode, respectively. Using the same electrolyte, the device achieved an energy density of 440 Wh·kg^{-1} and power density of 7.9 kW·kg^{-1}.

Until recently, only 10% of the theoretical capacity (617 mAh·g^{-1}) was accessible in rechargeable alkaline batteries. However, an important improvement has been recently achieved with a class of Bi-birnessite (a layered manganese oxide polymorph mixed with bismuth oxide (Bi_2O_3)) cathodes intercalated with Cu^{2+} that deliver near-full two-electron capacity reversibly for more than 6000 cycles [196]. The addition of $MnSO_4$ to the electrolyte is known to passivate the electrode surface [197]. Recently, however, a chemical conversion reaction mechanism between α-MnO_2 and H^+ was evidenced when mild aqueous $ZnSO_4$-based solution was used as the electrolyte in a Zn/MnO_2 battery [198]. As a result, the capacity of this battery was 285 mAh·g^{-1} (MnO_2), with capacity retention of 92% over 5000 cycles. These recent results show that the problems of the Zn/MnO_2 battery (limited cycling life and power) have now been entirely solved. Therefore, the alkaline Zn/MnO_2 batteries now outperform the Li-ion batteries not only by the lower price, but also by their performance, both in energy and in power density.

The future of MnO_2 as a supercapacitor element looks also bright. A composite with a core made of N-doped hollow carbon spheres (NHCS) and a shell composed of hierarchical birnessite-type MnO_2 nanoflakes was used as an anode for an asymmetric supercapacitor equipped with an NHCS cathode [199]. This supercapacitor in 1 mol·L^{-1} Na_2SO_4 aqueous electrolyte operated in the voltage range 0–1.8 V, delivering an energy density of 26.8 Wh·kg^{-1} at a power density of 233 W·kg^{-1} with minimal capacitance drop (4.8%) and 100% coulombic efficiency over 4000 cycles. Comparable results were found with an asymmetric supercapacitor based on a MnO_2 nanoflake/carbon nanotube core-shell particle composite [170]. We can thus conclude that MnO_2 now has great potential for energy conversion and storage applications.

Still, further improvements are predictable in the near future. It will be difficult to increase the energy density since we have already mentioned that its experimental value is close to theoretical for the most advanced electrodes [200], but the power density can still be improved by working on the porosity of the electrode material. For this purpose, synergetic effects between the research on batteries and the research on supercapacitors is expected as porosity increases the effective surface area with the electrolyte, which implies an increase of the power density, provided that the solid-electrolyte interface (SEI) is well controlled; porosity is also desired for capacitive electrodes [201–203]. A capacitance larger than 200 F·g^{-1} has already been obtained with mesoporous MnO_2 nanosheets [204]. Electrodes with optimized porosity should then also be built to increase the power density.

As we just mentioned, however, this increase of the effective surface area in contact with the electrolyte will be efficient only if the SEI is well controlled. Therefore, further studies should be

devoted to the investigation of the interface between MnO_2 and its environment. The coating of the particles, which can be used to increase the electrical conductivity and to protect the particle, is presumably perfectible. We have persisted in this review with structural properties that are so important to determine the rechargeability of the MnO_2-based devices. In particular, we have persisted with the role of K^+ ions on the physical and chemical properties of the DMO. In this context, further investigations should be useful to understand the role of different dopants on the morphology and the structural properties of MnO_2.

In their review on EMD batteries, Huang et al. [22] reported that engineers in the USA built a prototype EMD battery that can be rechargeable up to 90% within two minutes, and envisioned applications in electric cars. Actually, it is even overperforming for this purpose, because the grids cannot deliver such high power to recharge batteries. The maximum that the grids can deliver for private use without destabilization of the whole grid supply is the order of 50 kW·h. However, these high-power densities can be useful to solve the intermittence problems for integration of renewable energies on the grids.

All these improvements in the MnO_2 electrochemical properties and the performance already achieved make them already attractive and quite competitive with others and opens the route to high production, which should sustain further research along the lines mentioned above.

Acknowledgments: The authors greatly acknowledge Ahmed Bahloul, Ahmed Hashem, and Ashraf Abdel-Ghani for assisting with the experimental work.

Author Contributions: The authors contributed equally to the reported research and writing the paper.

Conflicts of Interest: The authors declare no conflicts of interest.

Abbreviations

The following abbreviations are used in this manuscript:

3D	three-dimensional
BET	Brunauer-Emmett-Teller
BTh	bithiophene
CMD	chemical manganese dioxide
CNT	carbon nanotubes
CTA	cetyltrimethylammonium
DEC	diethylcarbonate
DMC	dimethylcarbonate
DMSO	dimethyl sulfoxide
EA	electrocatalytic activity
EC	ethylenecarbonate
EDTA	ethylene diamine tetraacetate
EIS	electrochemical impedance spectroscopy
EMD	electrolytic manganese dioxide
EPR	electron paramagnetic resonance spectroscopy
EXAFS	extended X-ray absorption fine structure
FTIR	Fourier transform infrared
GNS	graphene nanosheets
GO	graphene oxide
hex.	hexagonal
HTMD	heat-treated manganese dioxide
HRTEM	high-resolution transmission electron microscopy
ICP	induced coupled plasma
ITO	indium tin oxide
MDO	manganese dioxide
MWCNT	multiwalled carbon nanotube

NHCS	N-doped hollow carbon spheres
NNs	nanoneedles
NUs	nanourchins
OMS	octahedral molecular sieve
ORR	oxygen reduction reaction
PBTh	polybithiophene
PEDOT	poly(3,4-ethylenedioxythiophene)
PEG	polyethylene glycol
PPy	polypyrrole
PTFE	polytetrafluoroethylene (Teflon)
PVA	poly(vinyl alcohol)
PVP	polyvinyl pyrrolidone
RT	room temperature
SCE	standard calomel electrode
SDS	sodium dodecyl-sulfate
SEM	scanning electron microscopy
TEM	transmission electron microscopy
TGA	thermogravimetric analysis

References

1. Julien, C.M.; Mauger, A.; Vijh, A.; Zaghib, K. *Lithium Batteries: Science and Technology*; Springer: Heidelberg, Germany, 2016.
2. Chalmin, E.; Vignaud, C.; Salomon, H.; Farges, F.; Susini, J.; Menu, M. Minerals discovered in Paleolithic black pigments by transmission electron microscopy and micro-X-ray absorption near-edge structure. *Appl. Phys. A* **2006**, *83*, 213–218. [CrossRef]
3. Saputra, E.; Muhammad, S.; Sun, H.; Ang, H.M.; Tade, M.O.; Wang, S. Different crystallographic one-dimensional MnO_2 nanomaterials and their superior performance in catalytic phenol degradation. *Environ. Sci. Technol.* **2013**, *47*, 5882–5887. [CrossRef] [PubMed]
4. Walter, M.G.; Warren, E.L.; McKone, J.R.; Boettcher, S.W.; Mi, Q.; Santoni, E.A.; Lewis, N.S. Solar water splitting cells. *Chem. Rev.* **2010**, *110*, 6446–6473. [CrossRef] [PubMed]
5. Zhu, Y.; Shen, M.; Xia, Y.; Lu, M. Au/MnO_2 nanostructured catalysts and their catalytic performance for the oxidation of 5-(hydroxymethyl)furfural. *Catal. Commun.* **2015**, *64*, 37–43. [CrossRef]
6. Zhang, Q.-X.; Peng, D.; Huang, X.-J. Effect of morphology of α-MnO_2 nanocrystals on electrochemical detection of toxic metal ions. *Electrochem. Commun.* **2013**, *34*, 270–273. [CrossRef]
7. Suib, SL. Porous manganese oxide octahedral molecular sieves and octahedral layered materials. *Acc. Chem. Res.* **2008**, *41*, 479–487. [CrossRef] [PubMed]
8. Liu, J.; Meng, L.; Fei, Z.; Dyson, P.J.; Jing, X.; Liu, X. MnO_2 nanosheets as an artificial enzyme to mimic oxidase for rapid and sensitive detection of glutathione. *Biosens. Bioelectron.* **2017**, *90*, 69–74. [CrossRef] [PubMed]
9. Chabre, Y.; Pannetier, J. Structural and electrochemical properties of the proton/γ-MnO_2 system. *Prog. Solid State Chem.* **1995**, *23*, 1–130. [CrossRef]
10. Hashem, A.M.; Abdel-Latif, A.M.; Abuzeid, H.M.; Abbas, H.M.; Ehrenberg, H.; Farag, R.S.; Mauger, A.; Julien, C.M. Improvement of the electrochemical performance of nanosized α-MnO_2 used as cathode material for Li-batteries by Sn-doping. *J. Alloys Compd.* **2011**, *509*, 9669–9674. [CrossRef]
11. Zhang, R.; Yu, X.; Nam, K.-W.; Ling, C.; Arthur, T.S.; Song, W.; Knapp, A.M.; Ehrlich, S.N.; Yang, X.-Q.; Matsui, M. α-MnO_2 as a cathode material for rechargeable Mg batteries. *Electrochem. Commun.* **2012**, *23*, 110–113. [CrossRef]
12. Rasul, S.; Suzuki, S.; Yamaguchi, S.; Miyayama, M. Manganese oxide octahedral molecular sieves as insertion electrodes for rechargeable Mg batteries. *Electrochim. Acta* **2013**, *110*, 247–252. [CrossRef]
13. Julien, C.; Massot, M. Spectroscopic studies of the local structure in positive electrodes for lithium batteries. *Phys. Chem. Chem. Phys.* **2002**, *4*, 4226–4235. [CrossRef]
14. Bélanger, D.; Brousse, T.; Long, J.W. Manganese oxides: Battery materials make the leap to electrochemical capacitors. *ECS Interface* **2008**, *17*, 49–52.

15. Zhang, X.-Y.; Han, L.-Q.; Sun, S.; Wang, C.-Y.; Chen, M.-M. MnO_2/C composite electrodes free of conductive enhancer for supercapacitors. *J. Alloys Compd.* **2015**, *653*, 539–545. [CrossRef]
16. Zhang, Q.-H.; Li, S.-P.; Sun, S.-Y.; Yin, X.-S.; Yu, J.-G. Lithium selective adsorption on 1-D MnO_2 nanostructure ion-sieve. *Adv. Powder Technol.* **2009**, *20*, 432–437. [CrossRef]
17. Della-Puppa, L.; Komarek, M.; Bordas, F.; Bollinger, J.-C.; Joussein, E. Adsorption of copper, cadmium, lead and zinc onto a synthetic manganese oxide. *J. Colloid Interface Sci.* **2013**, *399*, 99–106. [CrossRef] [PubMed]
18. Julien, C.; Massot, M.; Poinsignon, C. Lattice vibrations of manganese oxides. Part I. Periodic structures. *Spectrochim. Acta A* **2004**, *60*, 689–700. [CrossRef]
19. Clearfield, A. Role of ion exchange in solid-state chemistry. *Chem. Rev.* **1988**, *88*, 125–148. [CrossRef]
20. Biswal, A.; Tripathy, B.C.; Sanjay, K.; Meyrick, D.; Subbaiah, T.; Minakshi, M. Influence of the microstructure and its stability on the electrochemical properties of EMD produced from a range of precursors. *J. Solid State Electrochem.* **2013**, *17*, 3191–3198. [CrossRef]
21. Biswal, A.; Tripathy, B.C.; Sanjay, K.; Subbaiah, T.; Minakshi, M. Electrolytic manganese dioxide (EMD): A perspective on worldwide production, reserves and its role in electrochemistry. *RSC Adv.* **2015**, *5*, 58255–58283. [CrossRef]
22. Huang, M.; Li, F.; Dong, F.; Zhang, Y.X.; Zhang, L.L. MnO_2-based nanostructures for high performance supercapacitors. *J. Mater. Chem. A* **2015**, *3*, 21380–23423. [CrossRef]
23. Julien, C.M.; Mauger, A.; Zaghib, K. Surface effects on electrochemical properties of nano-sized $LiFePO_4$. *J. Mater. Chem.* **2011**, *21*, 9955–9968. [CrossRef]
24. Vondrak, J.; Jakubec, I.; Bludska, J. Electrochemical insertion of lithium in manganese oxide. *J. Power Sources* **1985**, *14*, 141–147. [CrossRef]
25. Zhang, Y.; Mo, Y. Preparation of MnO_2 electrodes coated by Sb-doped SnO_2 and their effect on electrochemical performance for supercapacitor. *Electrochim. Acta* **2014**, *142*, 76–83. [CrossRef]
26. Feng, L.; Zhang, Y.; Wang, R.; Zhang, Y.; Bai, W.; Ji, S.; Xuan, Z.; Yang, J.; Zheng, Z.; Guan, H. Preparation of PPy-coated MnO_2 hybrid micromaterials and their improved cyclic performance as anode for lithium-ion batteries. *Nanoscale Res. Lett.* **2017**, *12*, 518. [CrossRef] [PubMed]
27. Devaraj, S.; Munichandraiah, N. High capacitance of electrodeposited MnO_2 by the effect of a surface-active agent. *Electrochem. Solid-State Lett.* **2005**, *8*, A373–A377. [CrossRef]
28. Chou, S.-L.; Wang, J.-Z.; Chew, S.-Y.; Liu, H.-K.; Dou, S.-X. Electrodeposition of MnO_2 nanowires on carbon nanotube paper as free-standing, flexible electrode for supercapacitors. *Electrochem. Commun.* **2008**, *10*, 1724–1727. [CrossRef]
29. Livage, J.; Sanchez, C.; Henry, M.; Doeuff, S. The chemistry of the sol-gel process. *Solid State Ion.* **1989**, *32–33*, 633–638. [CrossRef]
30. Yu, P.; Zhang, X.; Wang, D.; Wang, L.; Ma, Y. Shape controlled synthesis of 3D hierarchical MnO_2 nanostructures for electrochemical supercapacitors. *Cryst. Growth Des.* **2009**, *9*, 528–533. [CrossRef]
31. Liu, X.; Chen, C.; Zhao, Y.; Jia, B. A review on the synthesis of manganese oxide nanomaterials and their applications on lithium-ion batteries. *J. Nanomater.* **2013**, *2013*, 736375. [CrossRef]
32. Wang, X.; Li, Y. Selected-control hydrothermal synthesis of α- and β-MnO_2 single crystal nanowires. *J. Am. Chem. Soc.* **2002**, *124*, 2880–2881. [CrossRef] [PubMed]
33. Wei, M.; Konishi, Y.; Zhou, H.; Sugihara, H.; Arakawa, H. Synthesis of single-crystal manganese dioxide nanowires by a soft chemical process. *Nanotechnology* **2005**, *16*, 245–249. [CrossRef] [PubMed]
34. Yuan, Z.Y.; Ren, T.Z.; Du, G.H.; Su, B.L. Facile preparation of single-crystalline nanowires of γ-MnOOH and β-MnO_2. *Appl. Phys. A* **2005**, *80*, 743–747. [CrossRef]
35. Sugantha, M.; Ramakrishnan, P.A.; Hermann, A.M.; Ginley, D.S. Nanostructured MnO_2 for Li batteries. *Int. J. Hydrogen Energy* **2003**, *28*, 597–600. [CrossRef]
36. Cui, H.J.; Huang, H.Z.; Fu, M.L.; Yuan, B.L.; Pearl, W. Facile synthesis and catalytic properties of single crystalline β-MnO_2 nanorods. *Catal. Commun.* **2011**, *12*, 1339–1343. [CrossRef]
37. Jana, S.; Pande, S.; Kumar-Sinha, A.; Sarkar, S.; Pradhan, M.; Basu, M.; Saha, S.; Pal, T. A green chemistry approach for the synthesis of flower-like Ag-doped MnO_2 nanostructures probed by surface-enhanced Raman spectroscopy. *J. Phys. Chem. C* **2009**, *113*, 1386–1392. [CrossRef]

38. Zhai, W.; Wang, C.; Yu, P.; Wang, Y.; Mao, L. Single-layer MnO_2 nanosheets suppressed fluorescence of 7-hydroxycoumarin: Mechanistic study and application for sensitive sensing of ascorbic acid in vivo. *Anal. Chem.* **2014**, *86*, 12206–12213. [CrossRef] [PubMed]
39. Wei, C.; Yu, L.; Cui, C.; Lin, J.; Wei, C.; Mathews, N.; Huo, F.; Sritharan, T.; Xu, Z. Ultrathin MnO_2 nanoflakes as efficient catalysts for oxygen reduction reaction. *Chem. Commun.* **2014**, *50*, 7885–7888. [CrossRef] [PubMed]
40. Sun, P.; Yi, H.; Peng, T.; Jing, Y.; Wang, R.; Wang, H.; Wang, X. Ultrathin MnO_2 nanoflakes deposited on carbon nanotube networks for symmetrical supercapacitors with enhanced performance. *J. Power Sources* **2017**, *341*, 27–35. [CrossRef]
41. Luo, J.; Zhu, H.T.; Fan, H.M.; Liang, J.K.; Shi, H.L.; Rao, G.H.; Li, J.B.; Du, Z.M.; Shen, Z.X. Synthesis of single-crystal tetragonal α-MnO_2 nanotubes. *J. Phys. Chem. C* **2008**, *112*, 12594–12598. [CrossRef]
42. Zheng, D.; Sun, S.; Fan, W.; Yu, H.; Fan, C.; Cao, G.; Yin, Z.; Song, X. One-step preparation of single-crystalline β-MnO_2 nanotubes. *J. Phys. Chem. B* **2005**, *109*, 16439–16443. [CrossRef] [PubMed]
43. Hashem, A.M.; Abdel-Ghany, A.E.; El-Tawil, R.; Bhaskar, A.; Hunzinger, B.; Ehrenberg, H.; Mauger, A.; Julien, C.M. Urchin-like α-MnO_2 formed of nano-needles for high-performance lithium batteries. *Ionics* **2016**, *22*, 2263–2271. [CrossRef]
44. Song, X.; Zhao, Y.; Zheng, Y. Synthesis of MnO_2 nanostructures with sea urchin shapes by a sodium dodecyl sulfate-assisted hydrothermal process. *Cryst. Growth Des.* **2007**, *7*, 159–162. [CrossRef]
45. Ragupathy, P.; Vasan, H.N.; Munichandraiah, N. Synthesis and characterization of nano-MnO_2 for electrochemical supercapacitor studies. *J. Electrochem. Soc.* **2008**, *155*, A34–A40. [CrossRef]
46. Aghazadeh, M.; Maragheh, M.G.; Ganjali, M.R.; Norouzi, P.; Faridbod, F. Electrochemical preparation of MnO_2 nanobelts through pulse base-electrogeneration and evaluation of their electrochemical performance. *Appl. Surf. Sci.* **2016**, *364*, 141–147. [CrossRef]
47. Wang, N.; Cao, X.; Guo, L.; Yang, S. λ-MnO_2 nanodisks and their magnetic properties. *Nanotechnology* **2007**, *18*, 475605. [CrossRef]
48. Lei, Z.; Zhang, J.; Zhao, X.S. Ultrathin MnO_2 nanofibers grown on graphitic carbon spheres as high-performance asymetric supercapacitor electrodes. *J. Mater. Chem.* **2012**, *22*, 153–160. [CrossRef]
49. Bahloul, A. Synthèse, Caractérisation et utilisation de matériaux composites à base de POC + MnO_2 comme matériaux d'électrodes dans les piles Zn-MnO_2. Ph.D. Thesis, Université Ferhat Abbas, Sétif, Algeria, 2011.
50. Bach, S.; Henry, M.; Baffier, N.; Livage, J. Sol-gel synthesis of manganese oxides. *J. Solid State Chem.* **1990**, *88*, 325–333. [CrossRef]
51. Hashem, A.M.; Abuzeid, H.M.; Abdel-Latif, A.M.; Abbas, H.M.; Ehrenberg, H.; Indris, S.; Mauger, A.; Groult, H.; Julien, C.M. MnO_2 nanorods prepared by redox reaction as cathodes in lithium batteries. *ECS Trans.* **2013**, *50*, 125–130. [CrossRef]
52. Tang, N.; Tian, X.; Yang, C.; Pi, Z.; Han, Q. Facile synthesis of α-MnO_2 nanorods for high-performance alkaline batteries. *J. Phys. Chem. Solids* **2010**, *71*, 258–262. [CrossRef]
53. Yin, B.; Zhang, S.; Jiang, H.; Qu, F.; Wu, X. Phase-controlled synthesis of polymorphic MnO_2 structures for electrochemical energy storage. *J. Mater. Chem.* **2015**, *3*, 5722–5729. [CrossRef]
54. Liu, Z.; Xu, K.; Sun, H.; Yin, S. One-step synthesis of single-layer MnO_2 nanosheets with multi-role sodium dodecyl sulfate for high performance pseudocapacitors. *Small* **2015**, *11*, 2182–2191. [CrossRef] [PubMed]
55. Jeong, Y.U.; Manthiram, A. Nanocrystalline manganese oxides for electrochemical capacitors with neutral electrolytes. *J. Electrochem. Soc.* **2002**, *149*, A1419–A1422. [CrossRef]
56. Kim, H.; Popov, B.N. Synthesis and characterization of MnO_2-based mixed oxides as supercapacitors. *J. Electrochem. Soc.* **2003**, *150*, D56–D62. [CrossRef]
57. Hernández, W.Y.; Centeno, M.A.; Romero-Sarria, F.; Ivanova, S.; Odriozola, J.A. Modified cryptomelane-type manganese dioxide nanomaterials for preferential oxidation of CO in the presence of hydrogen. *Catal. Today* **2010**, *157*, 160–165. [CrossRef]
58. Lee, H.Y.; Mannivanan, V.; Goodenough, J.B. Electrochemical capacitors with KCl electrolyte. *C. R. Acad. Sci. Ser. IIc* **1999**, *2*, 565–577. [CrossRef]
59. Komaba, S.; Kumagai, N.; Chiba, S. Synthesis of layered MnO_2 by calcination of $KMnO_4$ for rechargeable lithium battery cathode. *Electrochim. Acta* **2000**, *46*, 31–37. [CrossRef]
60. Alfaruqi, M.H.; Gim, J.; Kim, S.; Song, J.; Kim, J. A layered δ-MnO_2 nanoflake cathode with high zinc-storage capacities for eco-friendly battery applications. *Electrochem. Commun.* **2015**, *60*, 121–125. [CrossRef]

61. Subramanian, V.; Zhu, H.; Vajtai, R.; Ajayan, P.M.; Wei, B. Hydrothermal synthesis and pseudocapacitance properties of MnO_2 nanostructures. *J. Phys. Chem. B* **2005**, *109*, 20207–20214. [CrossRef] [PubMed]
62. Xiao, W.; Wang, D.; Lou, X.W. Shape-controlled synthesis of MnO_2 nanostructures with enhanced electrocatalytic activity for oxygen reduction. *J. Phys. Chem. C* **2010**, *114*, 1694–1700. [CrossRef]
63. Wang, H.; Lu, Z.; Qian, D.; Li, Y.; Zhang, W. Single-crystal α-MnO_2 nanorods: Synthesis and electrochemical properties. *Nanotechnology* **2007**, *18*, 115616. [CrossRef]
64. Wang, X.; Li, Y.D. Synthesis and formation mechanism of manganese dioxide nanowires/nanorods. *Chem. Eur. J.* **2003**, *9*, 300–306. [CrossRef] [PubMed]
65. Huang, K.; Lei, M.; Zhang, R.; Yang, H.J.; Yang, Y.G. Low-temperature route to dispersed manganese dioxide nanorods. *Mater. Lett.* **2012**, *78*, 202–204. [CrossRef]
66. Cheng, F.Y.; Chen, J.; Gou, X.L.; Shen, P.W. High-power alkaline Zn–MnO_2 batteries using γ-MnO_2 nanowires/nanotubes and electrolytic zinc powder. *Adv. Mater.* **2005**, *17*, 2753–2756. [CrossRef]
67. Ma, R.; Bando, Y.; Zhang, L.; Sasaki, T. Layered MnO_2 nanobelts: Hydrothermal synthesis and electrochemical measurement. *Adv. Mater.* **2004**, *16*, 918–922. [CrossRef]
68. Cheng, F.Y.; Zhao, J.Z.; Song, W.; Li, C.; Ma, H.; Chen, J.; Shen, P. Facile controlled synthesis of MnO_2 nanostructures of novel shapes and their application in batteries. *Inorg. Chem.* **2006**, *45*, 2038–2044. [CrossRef] [PubMed]
69. Gao, T.; Glerup, M.; Krumeich, F.; Nesper, R.; Fjellvag, H.; Norby, P. Microstructures and spectroscopic properties of cryptomelane-type manganese dioxide nanofibers. *J. Phys. Chem. C* **2008**, *112*, 13134–13140. [CrossRef]
70. Wang, X.; Lee, B.I.; Hu, M.Z.; Payzant, E.A.; Blom, D.A. Mechanism of nanocrystalline $BaTiO_3$ particles formation by hydrothermal refluxing synthesis. *J. Mater. Sci.* **2003**, *14*, 495–500.
71. Wang, X.H.; Ni, S.B.; Zhou, G.; Sun, X.L.; Yang, F.; Wang, J.M.; He, D. Facile synthesis of ultra-long α-MnO_2 nanowires and their microwave absorption properties. *Mater. Lett.* **2010**, *64*, 1496–1498. [CrossRef]
72. Wang, N.; Cao, X.; He, L.; Zhang, W.; Guo, L.; Chen, C.; Wang, R.; Yang, S. One-pot synthesis of highly crystallized λ-MnO_2 nanodisks assembled from nanoparticles: Morphology evolutions and phase transitions. *J. Phys. Chem. C* **2008**, *112*, 365–369. [CrossRef]
73. Villegas, J.C.; Garces, L.J.; Gomez, S.; Durand, J.P.; Suib, S.L. Particle size control of cryptomelane nanomaterials by use of H_2O_2 in acidic conditions. *Chem. Mater.* **2005**, *17*, 1910–1918. [CrossRef]
74. Trentler, T.J.; Hichman, K.M.; Goel, S.C.; Viano, A.M.; Gibbons, P.C.; Buhro, W.E. Solution-liquid-solid growth of crystalline III-V semiconductors: An analogy to vapor-liquid-solid growth. *Science* **1995**, *270*, 1791–1794. [CrossRef]
75. Xia, H.; Zhang, J.; Li, X. Synthesis of birnessite-type MnO_2 by the in-situ electrochemical oxidation of Mn_3O_4 film for supercapacitors. *Nanosc. Nanotechnol. Lett.* **2012**, *4*, 559–563. [CrossRef]
76. Li, Z.; Ding, Y.; Xiong, Y.; Xie, Y. Rational growth of various α-MnO_2 hierarchical structures and β-MnO_2 nanorods via a homogeneous catalytic route. *Cryst. Growth Des.* **2005**, *5*, 1953–1958. [CrossRef]
77. Kijima, N.; Yasuda, H.; Sato, T.; Yoshimura, Y. Preparation and characterization of open tunnel oxide α-MnO_2 precipitated by ozone oxidation. *J. Solid State Chem.* **2001**, *159*, 94–102. [CrossRef]
78. Luo, J.; Suib, S.L. Preparative parameters, magnesium effects, and anion effects in the crystallization of birnessites. *J. Phys. Chem. B* **1997**, *101*, 10403–10413. [CrossRef]
79. Feng, L.; Xuan, Z.; Zhao, H.; Bai, Y.; Guo, J.; Su, C.-W.; Chen, X. MnO_2 prepared by hydrothermal method and electrochemical performance as anode for lithium-ion battery. *Nanoscale Res. Lett.* **2014**, *9*, 290. [CrossRef] [PubMed]
80. Oaki, Y.; Imai, H. One-pot synthesis of manganese oxide nanosheets in aqueous solution: Chelation-mediated parallel control of reaction and morphology. *Angew. Chem. Int. Ed.* **2007**, *46*, 4951–4955. [CrossRef] [PubMed]
81. Tang, X.; Shan, X.; Li, S.; Liu, H.; Wu, X.; Chen, Y. Sol–gel process for the synthesis of ultrafine MnO_2 nanowires and nanorods. *Mater. Lett.* **2014**, *132*, 317–321. [CrossRef]
82. Kumar, H.; Sangwan, M.; Sangwan, P. Synthesis and characterization of MnO_2 nanoparticles using co-precipitation technique. *Int. J. Chem. Chem. Eng.* **2013**, *3*, 155–160.
83. Chen, S.; Zhu, J.; Han, Q.; Zheng, Z.; Yang, Y.; Wang, X. Shape-controlled synthesis of one-dimensional MnO_2 via a facile quick-precipitation procedure and its electrochemical properties. *Cryst. Growth Des.* **2009**, *9*, 4356–4361. [CrossRef]

84. Brousse, T.; Toupin, M.; Bélanger, D. Influence of microstucture on the charge storage properties of chemically synthesized manganese dioxide. *Chem. Mater.* **2002**, *14*, 3946–3952.
85. Toupin, M.; Brousse, T.; Bélanger, D. Charge storage mechanism of MnO_2 electrode used in aqueous electrochemical capacitor. *Chem. Mater.* **2004**, *16*, 3184–3190. [CrossRef]
86. Lee, H.Y.; Goodenough, J.B. Supercapacitor behavior with KCl electrolyte. *J. Solid State Chem.* **1999**, *144*, 220–223. [CrossRef]
87. Sagadevan, S. Investigations on synthesis, structural, morphological and dielectric properties of manganese oxides nanoparticles. *J. Mater. Sci. Eng.* **2015**, *4*, 1000172.
88. Barudžija, T.; Kusigerski, V.; Cvjetićanin, N.; Šorgić, S.; Perovic, M.; Mitrić, M. Structural and magnetic properties of hydrothermally synthesized β-MnO_2 and α-K_xMnO_2 nanorods. *J. Alloys Compd.* **2016**, *665*, 261–270. [CrossRef]
89. Barudžija, T.; Cvjetićanin, N.; Bajuk-Bogdanović, D.; Mojovic, M.; Mitrić, M. Vibrational and electron paramagnetic resonance spectroscopic studies of β-MnO_2 and α-K_xMnO_2 nanorods. *J. Alloys Compd.* **2017**, *728*, 259–270. [CrossRef]
90. Chen, Y.; Hong, Y.; Ma, Y.; Li, J. Synthesis and formation mechanism of urchin-like nano/micro-hybrid α-MnO_2. *J. Alloys Compd.* **2010**, *490*, 331–335. [CrossRef]
91. Sanchez-Botero, L.; Herrera, A.P.; Hinestroza, J.P. Oriented growth of α-MnO_2 nanorods using natural extracts from grape stems and apple peels. *Nanomaterials* **2017**, *7*, 117. [CrossRef] [PubMed]
92. Prasad, K.S.; Patra, A. Green synthesis of MnO_2 nanorods using phyllanthus amarus plant extract and their fluorescence studies. In *Green Processing and Synthesis*; Hessel, V., Ed.; De Gruyter GmbH: Berlin, Germany, 2017.
93. Jana, S.; Basu, S.; Pande, S.; Ghosh, S.K.; Pal, T. Shape-selective synthesis, magnetic properties, and catalytic activity of single crystalline β-MnO_2 nanoparticles. *J. Phys. Chem. C* **2007**, *111*, 16272–16277. [CrossRef]
94. Sui, N.; Duan, Y.; Jiao, X.; Chen, D. Large-scale preparation and catalytic properties of one-dimensional α/β-MnO_2 nanostructures. *J. Phys. Chem. C* **2009**, *113*, 8560–8565. [CrossRef]
95. Ching, S.; Welch, E.J.; Hughes, S.M.; Bahadoor, A.B.F.; Suib, S.L. Nonaqueous sol-gel syntheses of microporous manganese oxides. *Chem. Mater.* **2002**, *14*, 1292–1299. [CrossRef]
96. Liu, Z.; Xu, K.; She, P.; Yin, S.; Zhu, X.; Sun, H. Self-assembly of 2D MnO_2 nanosheets into high-purity aerogels with ultralow density. *Chem. Sci.* **2016**, *7*, 1926–1932. [CrossRef]
97. Julien, C.; Massot, M.; Rangan, S.; Lemal, M.; Guyomard, D. Study of the structural defects in γ-MnO_2 by Raman spectroscopy. *J. Raman Spectrosc.* **2002**, *33*, 223–228. [CrossRef]
98. Minakshi-Sundaram, M.; Biswal, A.; Mitchell, D.; Jones, R.; Fernandez, C. Correlation among physical and electrochemical behaviour of nanostructured electrolytic manganese dioxide from leach liquor and synthetic for aqueous asymmetric capacitor. *Phys. Chem. Chem. Phys.* **2016**, *18*, 4711–4720. [CrossRef] [PubMed]
99. McBreen, J. The electrochemistry of β-MnO_2 and γ-MnO_2 in alkaline electrolyte. *Electrochim. Acta* **1975**, *20*, 221–225. [CrossRef]
100. Sarciaux, S.; Le Gal La sale, A.; Verbaere, A.; Piffard, Y.; Guyomard, D. γ-MnO_2 for Li batteries. Part I. γ-MnO_2: Relationships between synthesis conditions, material characteristics and performances in lithium batteries. *J. Power Sources* **1999**, *81–82*, 656–660. [CrossRef]
101. Malankar, H.; Umare, S.S.; Singh, K.; Sharma, M. Chemical composition and discharge characteristics of γ-MnO_2 prepared using manganese ore. *J. Solid State Electrochem.* **2010**, *14*, 71–82. [CrossRef]
102. Guidelines for the Disposal of Alkaline-Manganese Dioxide Cells. Available online: http://steatite.co.uk/assets/files/Batteries/Duracell_ATB-full.pdf (accessed on 7 February 2015).
103. Zhang, N.; Cheng, F.; Liu, J.; Wang, L.; Long, X.; Liu, X.; Li, F.; Chen, J. Rechargeable aqueous zinc-manganese dioxide batteries with high energy and power densities. *Nat. Commun.* **2017**, *8*, 405. [CrossRef] [PubMed]
104. Minakshi-Sundaram, M.; Singh, P.; Issa, T.; Thurgate, S.; De, M. Lithium insertion into manganese dioxide electrode in MnO_2/Zn aqueous battery. Part III. Electrochemical behavior of gamma-MnO_2 in aqueous lithium hydroxide electrolyte. *J. Power Sources* **2006**, *153*, 165–169. [CrossRef]
105. Minakshi-Sundaram, M. Lithium insertion into manganese dioxide electrode in MnO_2/Zn aqueous battery. Part II. Comparison of the behavior of EMD and battery grade MnO_2 in Zn | MnO_2. *J. Power Sources* **2004**, *138*, 319–322. [CrossRef]
106. Dai, J.; Li, S.F.Y.; Siow, K.S.; Gao, Z. Synthesis and characterization of the hollandite-type MnO_2 as a cathode material in lithium batteries. *Electrochim. Acta* **2000**, *45*, 2211–2217. [CrossRef]

107. Thackeray, M.M.; Rossouw, M.H.; Gummow, R.J.; Liles, D.C.; Pearce, K.; De Kock, A.; David, W.I.F.; Hull, S. Ramsdellite-MnO_2 for lithium batteries: The ramsdellite to spinel transformation. *Electrochim. Acta* **1993**, *38*, 1259–1267. [CrossRef]
108. Bach, S.; Pereira-Ramos, J.P.; Cachet, C.; Bode, M.; Yu, L.T. Effect of Bi doping on the electrochemical behavior of layered MnO_2 as lithium intercalation compound. *Electrochim. Acta* **1995**, *40*, 785–789. [CrossRef]
109. Yang, Y.; Xiao, L.; Zhao, Y.; Wang, F. Hydrothermal synthesis and electrochemical characterization of α-MnO_2 nanorods as cathode material for lithium batteries. *Int. J. Electrochem. Sci.* **2008**, *3*, 67–74.
110. Bahloul, A.; Nessark, B.; Briot, E.; Groult, H.; Mauger, A.; Zaghib, K.; Julien, C.M. Polypyrrole-covered MnO_2 as electrode material for hydrid supercapacitor. *J. Power Sources* **2013**, *240*, 267–272. [CrossRef]
111. Xu, M.; Kong, L.; Zhou, W.; Li, H. Hydrothermal synthesis and pseudocapacitance properties of α-MnO_2 hollow spheres and hollow urchins. *J. Phys. Chem. C* **2007**, *111*, 19141–19147. [CrossRef]
112. Wang, W.; Gao, Z.; Wang, J.; Wang, B.; Liu, Q.; Li, Z.; Mann, T.; Yang, P.; Zhang, M.; Liu, L. Synthesis of reduced graphene nanosheet/urchin-like manganese dioxide composite and high performance as supercapacitor electrode. *Electrochim. Acta* **2012**, *69*, 112–119. [CrossRef]
113. Zhao, S.; Liu, T.; Shi, D.; Zhang, Y.; Zeng, W.; Li, T.; Miao, B. Hydrothermal synthesis of urchin-like MnO_2 nanostructures and its electrochemical character for supercapacitor. *Appl. Surf. Sci.* **2015**, *351*, 862–868. [CrossRef]
114. Jung, K.-N.; Riaz, A.; Lee, S.-B.; Lim, T.-H.; Park, S.-J.; Song, R.-H.; Yoon, S.; Shin, K.H.; Lee, J.-W. Urchin-like α-MnO_2 decorated with Au and Pd as a bi-functional catalyst for rechargeable lithium-oxygen batteries. *J. Power Sources* **2013**, *244*, 328–335. [CrossRef]
115. Li, Z.; Gu, A.; Lou, Z.; Sun, J.; Zhou, Q.; Chan, K.Y. Facile synthesis of iron-doped hollow urchin-like MnO_2 for supercapacitors. *J. Mater. Sci.* **2017**, *52*, 4852–4865. [CrossRef]
116. Feng, X.M.; Yan, Z.Z.; Chen, N.N. Synthesis of hollow urchin-like MnO_2 via a facile hydrothermal method and its application in supercapacitors. *Chin. J. Inorg. Chem.* **2014**, *30*, 2509–2515.
117. Wang, Y.; Zhou, Q.M.; Huang, Z.; Tang, J.G.; Jiao, J.Q.; Wang, Y.X.; Liu, J.X.; Huang, L.J.; Belfiore, L.A. MnO_2 nano-urchin/graphene hybrid electrodes: Facile synthesis and enhanced supercapacitance performance. *J. Nanosci. Nanotechnol.* **2015**, *15*, 9892–9898. [CrossRef] [PubMed]
118. Zhang, X.; Sun, X.; Zhang, H.; Zhang, D.; Ma, Y. Microwave-assisted reflux rapid synthesis of MnO_2 nanostructures and their application in supercapacitors. *Electrochim. Acta* **2013**, *87*, 637–644. [CrossRef]
119. Wang, M.X.; Tab, W.F.; Feng, X.H.; Koopal, L.K.; Liu, M.M.; Liu, F. One-step synthesis of sea urchin-like α-MnO_2 using KIO_4 as the oxidant and its oxidation of arsenite. *Mater. Lett.* **2012**, *77*, 60–62. [CrossRef]
120. Huang, X.K.; Lv, D.P.; Yue, H.J.; Attia, A.; Yang, Y. Controllable synthesis of α- and β-MnO_2: Cationic effect on hydrothermal crystallization. *Nanotechnology* **2008**, *19*, 225606–225612. [CrossRef] [PubMed]
121. Li, Z.Q.; Ding, Y.; Xiong, Y.J.; Yang, Q.; Xie, Y. One-step solution-based catalytic route to fabricate novel α-MnO_2 hierarchical structures on a large scale. *Chem. Commun.* **2005**, 918–920.
122. Yuan, Y.; Wood, S.M.; He, K.; Yao, W.; Tompsett, D.; Lu, J.; Nie, A.; Islam, M.S.; Shahbazian-Yassar, R. Atomistic insights into the oriented attachment of tunnel-based oxide nanostructures. *ACS Nano* **2016**, *10*, 539–548. [CrossRef] [PubMed]
123. Li, B.; Rong, G.; Xie, Y.; Huang, L.; Feng, C. Low-temperature synthesis of α-MnO_2 hollow urchins and their application in rechargeable Li^+ batteries. *Inorg. Chem.* **2006**, *45*, 6404–6410. [CrossRef] [PubMed]
124. He, W.; Yang, W.; Wang, C.; Deng, X.; Liu, B.; Xu, X. Morphology-controlled syntheses of α-MnO_2 for electrochemical energy storage. *Phys. Chem. Chem. Phys.* **2016**, *18*, 15235–15243. [CrossRef] [PubMed]
125. Radich, J.G.; Chen, Y.S.; Kamat, P.V. Nickel-doped MnO_2 nanowires anchored onto reduced graphene oxide for rapid cycling cathode in lithium ion batteries. *ECS J. Solid State Sci. Technol.* **2013**, *2*, M3178–M3181. [CrossRef]
126. Yoo, H.N.; Park, D.H.; Hwang, S.J. Effects of vanadium- and iron-doping on crystal morphology and electrochemical properties of 1D nanostructured manganese oxides. *J. Power Sources* **2008**, *185*, 1374–1379. [CrossRef]
127. Yang, D. Pulsed laser deposition of cobalt-doped manganese oxide thin films for supercapacitor applications. *J. Power Sources* **2012**, *198*, 416–422. [CrossRef]

128. Li, Q.; Yin, L.W.; Li, Z.Q.; Wang, X.K.; Qi, Y.X.; Ma, J.Y. Copper doped hollow structured manganese oxide mesocrystals with controlled phase structure and morphology as anode materials for lithium ion battery with Improved electrochemical performance. *ACS Appl. Mater. Interfaces* **2013**, *5*, 10975–10984. [CrossRef] [PubMed]
129. Wei, W.; Cui, X.; Chen, W.; Ivey, D.G. Manganese oxide-based materials as electrochemical supercapacitor electrodes. *Chem. Soc. Rev.* **2011**, *40*, 1697–1721. [CrossRef] [PubMed]
130. Kang, J.; Hirata, A.; Kang, L.; Zhang, X.; Hou, Y.; Chen, L.; Li, C.; Fujita, T.; Akagi, K.; Chen, M. Enhanced supercapacitor performance of MnO_2 by Atomic Doping. *Angew. Chem. Int. Ed.* **2013**, *52*, 1664–1667. [CrossRef] [PubMed]
131. King'ondu, C.K.; Opembe, N.; Chen, C.; Ngala, K.; Huang, H.; Iyer, A.; Garcés, H.F.; Suib, S.L. Manganese oxide octahedral molecular sieves (OMS-2) multiple framework substitutions: A new route to OMS-2 particle size and morphology control. *Adv. Funct. Mater.* **2011**, *21*, 312–323. [CrossRef]
132. Tseng, L.-T.; Lu, Y.; Fan, H.M.; Wang, Y.; Luo, X.; Liu, T.; Munroe, P.; Li, S.; Yi, J. Magnetic properties in α-MnO_2 doped with alkaline elements. *Sci. Rep.* **2015**, *5*, 9094. [CrossRef] [PubMed]
133. Lee, J.; Ju, J.B.; Cho, W.; Cho, B.; Oh, S. Todorokite-type MnO_2 as a zinc-ion intercalating material. *Electrochim. Acta* **2013**, *112*, 138–143. [CrossRef]
134. Liu, Q.; Wang, S.; Cheng, H. High rate capabilities Fe-doped EMD electrodes for Li/MnO_2 primary battery. *Int. J. Electrochim. Sci.* **2013**, *8*, 10540–10548.
135. Alfaruqi, M.H.; Islam, S.; Mathew, V.; Song, J.; Kim, S.; Tung, D.P.; Jo, J.; Kim, S.; Baboo, J.P.; Xiu, Z.; et al. Ambient redox synthesis of vanadium-doped manganese dioxide nanoparticles and their enhanced zinc storage properties. *Appl. Surf. Sci.* **2017**, *404*, 435–442. [CrossRef]
136. Lambert, T.N.; Vigil, J.A.; White, S.E.; Delker, C.J.; Davis, D.J.; Kelly, M.; Brumbach, M.T.; Rodriguez, M.A.; Swartzentruber, B.S. Understanding the effects of cationic dopants on α-MnO_2 oxygen reduction reaction electrocatalysts. *J. Phys. Chem. C* **2017**, *121*, 2789–2797. [CrossRef]
137. Hao, J.; Liu, Y.; Shen, H.; Li, W.; Li, J.; Li, Y.; Chen, Q. Effect of nickel-ion doping in MnO_2 nanoneedles as electrocatalyst for the oxygen reduction reaction. *J. Mater. Sci. Mater. Electron.* **2016**, *27*, 6598–6605. [CrossRef]
138. Calegaro, M.; Lima, F.; Ticianelli, E. Oxygen reduction reaction on nanosized manganese oxide particles dispersed on carbon in alkaline solutions. *J. Power Sources* **2006**, *158*, 735–739. [CrossRef]
139. Davis, D.J.; Lambert, T.N.; Vigil, J.A.; Rodriguez, M.A.; Brumbach, M.T.; Coker, E.N.; Limmer, S.J. Role of Cu-ion doping in Cu-α-MnO_2 nanowire electrocatalysts for the oxygen reduction reaction. *J. Phys. Chem. C* **2014**, *118*, 17342–17350. [CrossRef]
140. Hu, Z.; Xiao, X.; Chen, C.; Li, T.; Huang, L.; Zhang, C.; Su, J.; Miao, L.; Jiang, J.; Zhang, Y.; et al. Al-doped α-MnO_2 for high mass-loading pseudocapacitor with excellent stability. *Nano Energy* **2015**, *11*, 226–234. [CrossRef]
141. Gobi, R.; Poonguzhali, R.; Shanmugam, N.; Kumar, A.S.; Shamugam, R.; Sathishkumar, K. Influence of Zn doping on electrochemical capacitor behaviour of MnO_2 nanocrystals. *RSC Adv.* **2015**, *5*, 45407–45415.
142. Chen, K.; Pan, W.; Xue, D. Phase transformation of Cr^{3+}-doped MnO_2 for pseudocapacitive electrode marerials. *J. Phys. Chem. C* **2016**, *120*, 20077–20081. [CrossRef]
143. Poonguzhali, R.; Gobi, R.; Shanmugam, N.; Kumar, A.S.; Viruthagiri, G.; Kannadasan, N. Enhancement in electrochemical behavior of copper doped MnO_2 electrode. *Mater. Lett.* **2015**, *157*, 116–122. [CrossRef]
144. Hu, Z.; Xiao, X.; Huang, L.; Chen, C.; Li, T.; Su, T.; Cheng, X.; Miao, L.; Zhang, Y.; Zhou, J. 2D vanadium doped manganese dioxides nanosheets for pseudocapacitive energy storage. *Nanoscale* **2015**, *7*, 16094–16099. [CrossRef] [PubMed]
145. Gulbinska, M.K.; Suib, S.L. Vanadium-substituted porous manganese oxides with Li-ion intercalation properties. *J. Power Sources* **2011**, *196*, 2149–2154. [CrossRef]
146. Zeng, J.; Wang, S.; Liu, Q.; Lei, X. High-capacity V-/Sc-/Ti-doped MnO_2 for Li/MnO_2 batteries and structural changes at different discharge depths. *Electrochim. Acta* **2014**, *127*, 115–122. [CrossRef]
147. Wang, S.; Liu, Q.; Yu, J.; Zeng, J. Anisotropic expansion and high rate discharge performance of V-doped MnO_2 for Li/MnO_2 primary battery. *Int. J. Electrochim. Sci.* **2012**, *7*, 1242–1250.
148. Li, D.; Li, W.; Deng, Y.; Wu, X.; Han, N.; Chen, Y. Effective Ti doping of δ-MnO_2 via anion route for highly active catalytic combustion of benzene. *J. Phys. Chem. C* **2016**, *120*, 10275–10282. [CrossRef]

149. Jin, L.; Xu, L.; Morein, C.; Chen, C.; Lai, M.; Dharmarathna, S.; Dobley, A.; Suib, S.L. Titanium containing γ-MnO_2 (TM) hollow spheres: One-step synthesis and catalytic activities in Li/air batteries and oxidative chemical reaction. *Adv. Funct. Mater.* **2010**, *22*, 3373–3382. [CrossRef]
150. Pargoletti, E.; Cappelletti, G.; Minguzzi, A.; Rondinini, S.; Leoni, M.; Marelli, M.; Vertova, A. High-performance of bare and Ti-doped α-MnO_2 nanoparticles in catalyzing the oxygen reduction reaction. *J. Power Sources* **2016**, *325*, 116–128. [CrossRef]
151. Machefaux, E.; Brousse, T.; Belanger, D.; Guyomard, D. Supercapacitor behavior of new substituted manganese dioxides. *J. Power Sources* **2007**, *165*, 651–655. [CrossRef]
152. Hashem, A.M.; Abuzeid, H.M.; Narayanan, N.; Ehrenberg, H.; Julien, C.M. Synthesis, structure, magnetic, electrical and electrochemical properties of Al, Cu and Mg doped MnO_2. *Mater. Chem. Phys.* **2011**, *130*, 33–38. [CrossRef]
153. De Guzman, R.N.; Awaludin, A.; Shen, Y.F.; Tian, Z.R.; Suib, S.L.; Ching, S.; O'Young, C.L. Electrical resistivity measurements on manganese oxides with layer and tunnel structures: Birnessites, todorokites and cryptomelanes. *Chem. Mater.* **1995**, *7*, 1286–1292. [CrossRef]
154. Yu, X.L.; Wu, S.X.; Liu, Y.L.; Li, S.W. Electronic spectrum of a helically Hund-coupled β-MnO_2. *Solid State Commun.* **2008**, *146*, 166–168. [CrossRef]
155. Hashem, A.M.A.; Mohamed, H.A.; Bahloul, A.; Eid, A.E.; Julien, C.M. Thermal stabilization of tin- and cobalt-doped manganese dioxide. *Ionics* **2008**, *14*, 7–14. [CrossRef]
156. Abuzeid, H.M.; Hashem, A.M.; Narayanan, N.; Ehrenberg, H.; Julien, C.M. Nanosized silver-coated and doped manganese dioxide for rechargeable lithium batteries. *Solid State Ion.* **2011**, *182*, 108–115. [CrossRef]
157. Hashem, A.M.; Abuzeid, H.M.; Mikhailova, D.; Ehrenberg, H.; Mauger, A.; Julien, C.M. Structural and electrochemical properties of α-MnO_2 doped with cobalt. *J. Mater. Sci.* **2012**, *47*, 2479–2485. [CrossRef]
158. Tang, C.-L.; Wei, X.; Jiang, Y.-M.; Wu, X.-Y.; Han, L.-N.; Wang, K.-X.; Chen, J.S. Cobalt-doped MnO_2 hierarchical yolk-shell spheres with improved supercapacitive performance. *J. Phys. Chem. C* **2015**, *119*, 8465–8471. [CrossRef]
159. Korosec, R.C.; Umek, P.; Gloter, A.; Gomilsek, J.P.; Bukovec, P. Structural properties and thermal stability of cobalt- and chromium-doped α-MnO_2 nanorods. *Beilstein J. Nanotechnol.* **2017**, *8*, 1032–1042. [CrossRef] [PubMed]
160. Duan, Y.; Liu, Z.; Jing, H.; Zhang, Y.; Li, S. Novel microwave dielectric response of Ni/Co-doped manganese dioxides and their microwave absorbing properties. *J. Mater. Chem.* **2010**, *22*, 18291–18299. [CrossRef]
161. Kamimura, A.; Nozaki, Y.; Nishiyama, M.; Nakayama, M. Oxidation of benzyl alcohols by semi-stoichiometric amounts of cobalt-doped birnessite-type layered MnO_2 under oxygen atmosphere. *RSC Adv.* **2013**, *3*, 468–472. [CrossRef]
162. Biswal, A.; Minakshi Sundaram, M.; Tripathy, B. Electrodeposition of sea urchin and cauliflower-like nickel-/cobalt-doped manganese dioxide hierarchical nanostructures with improved energy-storage behavior. *ChemElectroChem* **2016**, *3*, 976–985. [CrossRef]
163. Boden, D.; Venuto, C.J.; Wisler, D.; Wylie, R.B. The alkaline manganese dioxide electrode: II. The charge process. *J. Electrochem. Soc.* **1968**, *115*, 333–338. [CrossRef]
164. Miyazaki, K. A change in relative concentration of oxygen during the discharge of MnO_2 in strong alkaline solution. *J. Electroanal. Chem.* **1971**, *21*, 414–418. [CrossRef]
165. McBreen, J. Bismuth oxide as an additive in pasted zinc electrodes. *J. Power Sources* **1985**, *15*, 169–170. [CrossRef]
166. Yao, Y.F.; Gupta, N.; Wroblowa, H.S. Rechargeable manganese oxide electrodes: Part I. Chemically modified materials. *J. Electroanal. Chem.* **1987**, *223*, 107–117. [CrossRef]
167. Im, D.; Manthiram, A.; Coffey, B. Manganese(III) chemistry in KOH solutions in the presence of Bi- or Ba-containing compounds and its implications on the rechargeability of γ-MnO_2 in alkaline cells. *J. Electrochem. Soc.* **2003**, *150*, A1651–A1659. [CrossRef]
168. Yu, L.T. Rechargeability of MnO_2 in KOH media produced by decomposition of dissolved $KMnO_4$ and $Bi(NO_3)_3$ mixtures. II. A reaction viewpoint on the role of Bi. *J. Electrochem. Soc.* **1997**, *144*, 802–809. [CrossRef]
169. Im, D.; Manthiram, A. Role of bismuth and factors influencing the formation of Mn_3O_4 in rechargeable alkaline batteries based on bismuth-containing manganese oxides. *J. Electrochem. Soc.* **2003**, *150*, A68–A73. [CrossRef]

170. Sundaram, M.; Singh, P. Synergistic effect of additives on electrochemical properties of MnO_2 cathode in aqueous rechargeable batteries. *J. Solid State Electrochem.* **2012**, *16*, 1487–1492.
171. Minakshi, M.; Mitchell, D.R.G.; Prince, K. Incorporation of TiB_2 additive into MnO_2 cathode and its influence on rechargeability in an aqueous battery system. *Solid State Ion.* **2008**, *179*, 355–361. [CrossRef]
172. Minakshi, M.; Nallathamby, K.; Mitchell, D.R.G. Electrochemical characterization of an aqueous lithium rechargeable battery: The effect of CeO_2 additions to the MnO_2 cathode. *J. Alloys Compd.* **2009**, *479*, 87–90. [CrossRef]
173. Minakshi, M.; Blackford, M.G.; Ionescu, M. Characterization of alkaline-earth oxide additions to the MnO_2 cathode in am aqueous secondary battery. *J. Alloys Compd.* **2011**, *509*, 5874–5980. [CrossRef]
174. Minakshi, M.; Blackford, M.G. Electrochemical characteristics of B_4C or BN added MnO_2 cathode material for alkaline batteries. *Mater. Chem. Phys.* **2010**, *123*, 700–705. [CrossRef]
175. Minakshi, M.; Mitchell, D.R.G. The influence of bismuth oxide doping on the rechargeability of aqueous cells using MnO_2 cathode and LiOH electrolyte. *Electrochim. Acta* **2008**, *53*, 6323–6327. [CrossRef]
176. Raghuveer, V.; Manthiram, A. Role of TiB_2 and Bi_2O_3 additives on the rechargeability of MnO_2 in alkaline cells. *J. Power Sources* **2006**, *163*, 598–603. [CrossRef]
177. Bahloul, A.; Nessark, B.; Briot, E.; Groult, H.; Mauger, A.; Julien, C.M. Polypyrrole-covered MnO_2 as electrode material for hydrid supercapacitor. *ECS Trans.* **2013**, *50*, 79–84. [CrossRef]
178. Zouaoui, H.; Abdi, D.; Bahloul, A.; Nessark, B.; Briot, E.; Groult, H.; Mauger, A.; Julien, C.M. Study of the electro-synthesis, characterization and photoconducting performance of polybithiophene/MnO_2 nanocomposite. *Mater. Sci. Eng. B* **2016**, *208*, 29–38. [CrossRef]
179. Bahloul, A.; Nessark, B.; Chelali, N.-E.; Groult, H.; Mauger, A.; Julien, C.M. New composite cathode material for Zn//MnO_2 cells obtained by electro-deposition of polybithiophene on manganese dioxide particles. *Solid State Ion.* **2011**, *204–205*, 53–60. [CrossRef]
180. Bahloul, A.; Nessark, B.; Habelhames, F.; Julien, C.M. Preparation and characterization of polybithiophene/β-MnO_2 composite electrode for oxygen reduction. *Ionics* **2011**, *17*, 239–246. [CrossRef]
181. Dai, Y.M.; Tang, S.C.; Peng, J.Q.; Chen, H.Y.; Ba, Z.X.; Ma, Y.J.; Meng, X.K. MnO_2@SnO_2 core-shell heterostructured nanorods for supercapacitors. *Mater. Lett.* **2014**, *130*, 107–110. [CrossRef]
182. Zhang, J.H.; Wang, Y.H.; Zang, J.B.; Xin, G.X.; Ji, H.Y.; Yuan, Y.G. Synthesis of MnO_2/short multi-walled carbon nanotube nanocomposite for supercapacitors. *Mater. Chem. Phys.* **2014**, *143*, 595–599. [CrossRef]
183. Jiang, H.; Ma, J.; Li, C. Mesoporous carbon incorporated metal oxide nanomaterials as supercapacitor electrodes. *Adv. Mater.* **2012**, *24*, 4197–4202. [CrossRef] [PubMed]
184. Cheng, Q.; Tang, J.; Ma, J.; Zhang, H.; Shinya, N.; Qin, L.-C. Graphene and nanostructured MnO_2 composite electrodes for supercapacitors. *Carbon* **2011**, *49*, 2917–2925. [CrossRef]
185. Lv, Q.; Wang, S.; Sun, H.; Luo, J.; Xiao, J.; Xiao, J.W.; Xiao, F.; Wang, S. Solid-state thin-film supercapacitors with ultrafast charge/discharge based on N-doped-carbon-tubes/Au-nanoparticles-doped-MnO_2 nanocomposites. *Nano Lett.* **2016**, *16*, 40–47. [CrossRef] [PubMed]
186. Fan, Z.; Yan, J.; Zhi, L.; Zhang, Q.; Wei, T.; Feng, J.; Zhang, M.; Qian, W.; Wei, F. A three-dimensional, carbon nanotube/graphene sandwich and its application as electrode in supercapacitors. *Adv. Mater.* **2010**, *22*, 3723–3728. [CrossRef] [PubMed]
187. Chen, S.; Zhu, J.; Wu, X.; Han, Q.; Wang, X. Graphene oxide–MnO_2 nanocomposites for supercapacitors. *ACS Nano* **2010**, *4*, 2822–2830. [CrossRef] [PubMed]
188. Song, H.; Li, X.; Zhang, Y.; Wang, H.; Li, H.; Huang, J. A nanocomposite of needle-like MnO_2 nanowires arrays sandwiched between graphene nanosheets for supercapacitors. *Ceram. Int.* **2014**, *40*, 1251–1255. [CrossRef]
189. Liu, R.; Duay, J.; Lee, S.B. Redox exchange induced MnO_2 nanoparticle enrichment in poly(3,4-ethylenedioxythiophene) nanowires for electrochemical energy storage. *ACS Nano* **2010**, *4*, 4299–4307. [CrossRef] [PubMed]
190. Long, J.W.; Rhodes, C.P.; Young, A.L.; Rolison, D.R. Ultrathin, protective coatings of poly(*o*-phenylenediamine) as electrochemical proton gates: Making mesoporous MnO_2 nanoarchitectures stable in acid electrolytes. *Nano Lett.* **2003**, *3*, 1155–1161. [CrossRef]
191. Yan, J.; Khoo, E.; Sumboja, A.; Lee, P.S. Facile coating of manganese oxide on tin oxide nanowires with high-performance capacitive behavior. *ACS Nano* **2010**, *4*, 4247–4255. [CrossRef] [PubMed]

192. Nakagawa, K.; Suzuki, K.; Kondo, M.; Hayakawa, S.; Nakayama, M. Electrosynthesis of layered organo-manganese dioxide framework-doped with cobalt for iodide sensing. *Langmir* **2017**, *33*, 4647–4653. [CrossRef] [PubMed]
193. Hashem, A.M.; Abuzeid, H.M.; Adbel-Ghany, A.E.; Mauger, A.; Zaghib, K.; Julien, C.M. SnO_2-MnO_2 composite powders and their electrochemical properties. *J. Power Sources* **2012**, *202*, 291–298. [CrossRef]
194. Zeng, Y.; Zhang, X.; Meng, Y.; Yu, M.; Yi, J.; Wu, Y.; Lu, X.; Tong, Y. Achieving ultra-high energy density and long durability in a flexible rechargeable quasi-solid-state Zn-MnO_2 battery. *Adv. Mater.* **2017**, *29*. [CrossRef] [PubMed]
195. Qiu, W.; You, A.; Zhang, Z.; Li, G.; Lu, X.; Tong, Y. High-performance flexible quasi-solid-state Zn-MnO_2 battery based on MnO_2 nanorod arrays coated 3D porous nitrogen-doped carbon cloth. *J. Mater. Chem. A* **2017**, *5*, 14838–14846. [CrossRef]
196. Chamoun, M.; Brant, W.R.; Karlsson, G.; Noréus, D. *In-Operando* investigation of rechargeable aqueous sulfate Zn/MnO_2 batteries. In Proceedings of the 231st ECS Meeting, New Orleans, LA, USA, 28 May–1 June 2017; The Electrochemical Society: Pennington, NJ, USA, 2017.
197. Pan, H.; Shao, Y.; Yan, P.; Cheng, Y.; Han, K.S.; Nie, Z.; Wang, C.; Yang, J.; Li, X.; Bhattacharya, P.; et al. Reversible aqueous zinc/manganese oxide energy storage from conversion reaction. *Nat. Energy* **2016**, *1*, 16039. [CrossRef]
198. Liu, T.; Jiang, C.; You, W.; Yu, J. Hierarchical porous C/MnO_2 composite hollow microspheres with enhanced capacitor performance. *J. Mater. Chem. A* **2017**, *5*, 8635–8643. [CrossRef]
199. Gueon, D.; Moon, J.H. MnO_2 nanoflake-shelled carbon nanotube particles for high-performance supercapacitors. *ACS Sustain. Chem. Eng.* **2017**, *5*, 2445–2453. [CrossRef]
200. Yan, D.; Guo, Z.; Zhu, G.; Yang, H.; Wei, R.; Xu, H.; Yu, A. Electrochemical properties of 3D MnO_2 films prepared by chemical bath deposition at room temperature. *Mater. Lett.* **2012**, *82*, 156–158. [CrossRef]
201. Zhu, T.; Zheng, S.; Chen, Y.; Luo, J.; Guo, H.; Chen, Y. Improvement of hydrothermally synthesized MnO_2 electrodes on Ni foams via facile annealing for supercapacitor applications. *J. Mater. Sci.* **2014**, *49*, 6118–6126. [CrossRef]
202. Deng, M.-J.; Chang, J.-K.; Wang, C.-C.; Chen, K.-W.; Lin, C.-M.; Tang, M.-T.; Chen, J.-M.; Lu, K.-T. High-performance electrochemical pseudo-capacitor based on MnO_2 nanowires/Ni foam as electrode with a novel Li-ion quasi-ionic liquid as electrolyte. *Energy Environ. Sci.* **2011**, *4*, 3942–3946. [CrossRef]
203. Yan, D.; Guo, Z.; Zhu, G.; Yu, Z.; Xu, H.; Yu, A. MnO_2 film with three-dimensional structure prepared by hydrothermal process for supercapacitor. *J. Power Sources* **2012**, *199*, 409–412. [CrossRef]
204. Kundu, M.; Liu, L. Direct growth of mesoporous MnO_2 nanosheet arrays on nickel foam current collectors for high-performance pseudocapacitors. *J. Power Sources* **2013**, *243*, 676–681. [CrossRef]

© 2017 by the authors. Licensee MDPI, Basel, Switzerland. This article is an open access article distributed under the terms and conditions of the Creative Commons Attribution (CC BY) license (http://creativecommons.org/licenses/by/4.0/).